INTERNATIONAL JOURNAL FOR NUMERICAL METHODS IN FLUIDS
Int. J. Numer. Meth. Fluids 2002; **38**:1133–1157 (DOI: 10.1002/fld.278)

2-D transmitral flows simulation by means of the immersed boundary method on unstructured grids

F. M. Denaro[1,*,†] and F. Sarghini[2]

[1]*Dipartimento di Ingegneria Aerospaziale, Seconda Universita' degli Studi di Napoli, Italia*
[2]*Dipartimento di Energetica Termofluidodinamica e Condizionamento Ambientale, Universita' degli Studi di Napoli Federico II, Italia*

SUMMARY

Interaction between computational fluid dynamics and clinical researches recently allowed a deeper understanding of the physiology of complex phenomena involving cardio-vascular mechanisms. The aim of this paper is to develop a simplified numerical model based on the Immersed Boundary Method and to perform numerical simulations in order to study the cardiac diastolic phase during which the left ventricle is filled with blood flowing from the atrium throughout the mitral valve. As one of the diagnostic problems to be faced by clinicians is the lack of a univocal definition of the diastolic performance from the velocity measurements obtained by Eco–Doppler techniques, numerical simulations are supposed to provide an insight both into the physics of the diastole and into the interpretation of experimental data. An innovative application of the Immersed Boundary Method on unstructured grids is presented, fulfilling accuracy requirements related to the development of a thin boundary layer along the moving immersed boundary. It appears that this coupling between unstructured meshes and the Immersed Boundary Method is a promising technique when a wide range of spatial scales is involved together with a moving boundary. Numerical simulations are performed in a range of physiological parameters and a qualitative comparison with experimental data is presented, in order to demonstrate that, despite the simplified model, the main physiological characteristics of the diastole are well represented.

KEY WORDS: immersed boundary method; unstructured grid; fractional time-step method; mitral flow analysis; diastolic function

1. INTRODUCTION

At present, the diastolic dysfunction is considered a primary mechanism in the pathogenesis of the cardiac congestion and it appears to be also one of the earliest detectable alterations in many pathological conditions of the heart [1, 2]. Therefore, immediate and adequate therapies could sensibly improve the diastolic performance as well as they could also avoid the

*Correspondence to: F. M. Denaro, Dipartimento di Ingegneria Aerospaziale, Seconda Universita di Napoli, Via Roma 29, 81031 Aversa (Ce), Italy.
†E-mail: denaro@unina.it

Received January 2000
Revised October 2001

consequent overload in the systolic function. An accurate diagnostic tool is based on the direct measurement of intra-cardiac pressure but this is obtainable only by means of cardiac catheterism. This latter is a kind of investigation both expensive and not completely risk-free for the patient; for this reason, it is often preferable to use a non-invasive diagnostic process, based on the analysis of measurable data (i.e. velocity patterns) related to the ventricular filling and to the haemodynamics parameters of the diastolic function [3, 4]. Unfortunately, all non-invasive techniques are not able to provide a direct measurement of the pressure, which is a necessary parameter to characterize the diastolic function. Thus, the velocity measurements can give only a partial representation of the ventricular filling rather than provide a comprehensive chart of indexes of the actual performance [1–4] in diastole.

While the knowledge of some physiological parameters, measured by catheterism (i.e. compliance and relaxation), leads to a univocal interpretation of the ventricular filling, the opposite is not always true (the so-called *reverse problem of the diastole*). As a consequence of a non-invasive diagnostic process, the analysis of the ventricular filling cannot provide such requested univocal interpretation of the diastolic performance. In fact, occasionally, observations of *pseudo-normal* velocity patterns confirm that different conditions of the diastolic performance (i.e. pressure levels and compliance) can originate the same appearance of the filling.

Such a non-univocal definition of the reverse diastolic problem generates uncertainties in adopting Doppler measurement, which is one of the most used tools in non-invasive diagnostic processes. Although the pulsating Doppler echocardiography allows clinicians to measure flow velocities both throughout the mitral valve and the pulmonary veins, any modification of these measurements results as a consequence of complex interactions between pressure and ventricular volumes and the hope of clinicians is to be able to correlate these distinct appearances. Often, they consider the correlation between velocity and pressure that is provided by the Bernoulli equation but the hypotheses required for considering valid such an equation are quite far to be accomplished in the cardiac fluid dynamics. Furthermore, the Doppler measurement is related only to the averaged stream-wise flow component thus, lack of multi-dimensional information can add some confusion in the clinical interpretation.

As a matter of fact, the blood motion is governed by the solution of the unsteady Navier–Stokes (NS) equations, the Bernoulli equation being appropriate only for very simple cases. In this paper the blood is considered to be a Newtonian fluid, as proposed by Pedley [5]; this assumption is based on the hypothesis that, with exception of micro-circulation, blood has a Newtonian behaviour when shear rate grows up (it is generally accepted that plasma behaves as a Newtonian fluid in physiological conditions). In the case of constant fluid density, as it can be also assumed for the blood [5], the pressure in the numerical solution of NS equations is not considered as a thermodynamics variable but it is determined as a scalar function from the enforcement of the continuity equation and it depends on an arbitrary function of time.

Many potentialities, offered to clinicians by the Computational Fluid Dynamics (CFD), have been only partially exploited although some methodologies of CFD have been already presented and applied in a series of papers by Peskin *et al.* [6–12] where 2-D and 3-D simulations are illustrated in the framework of the *Immersed Boundary* (IB) Method. In such simulations, among other various problems, trans-mitral flows were studied in order to provide a support to clinicians in testing prosthetic valve efficiency. Some other examples of computational methodologies, for studying the diastole, were shown by Yellin *et al.* in Reference [1] while simpler mathematical models were proposed by Thomas *et al.* in

Reference [2]. They analysed the pathological relevance of modifications of some physiological parameters that are measured by the Doppler echocardiography and the main target was to provide a clear indication of the actual diastolic function by means of one or more global performance indexes.

Numerical simulations of such flows are of great relevance in supporting clinicians and realistic simulations should take into account both a physiological Reynolds number and the elastic properties of the fibres along with an accurate description of the time varying properties of them.

Unfortunately, owing to the complexity of the problem, the difficulties in performing accurate simulations come along with the fact that clinical diagnosis does not provide the knowledge of many parameters required for defining the boundary conditions. It results, for example, that no point-wise velocities are measured onto the boundary of the domain: flow rate of pulmonary veins, mean pressure in atrium (but only with catheterism), atrial and ventricular volume deformations (obtained by NMR) are some of the measurable quantities that can be exploited in order to formulate approximate numerical boundary conditions. Therefore, a simplified model in which some approximate boundary conditions can be properly applied, is tested in this paper.

In fact, a 2-D equivalent geometry is decomposed by an unstructured tessellation and, by adopting the IB method, the discrete NS equations for incompressible flows are solved. In the 2-D model, the dynamic of the mitral valve is simulated by considering each leaflet as a chain of elastic links, as also proposed in References [6] and [9], a formulation in which the material line, immersed in the fluid, acts as a local source of additional stresses, leading to a complex solid–fluid dynamics interaction. The application of an unstructured grid is motivated by the necessity of resolving the known accuracy problems in adopting the IB method when a thin boundary layer develops along the immersed boundary [12]. Although the approach on a structured grid is probably simpler to implement, as long as a local refinement is not required, the unstructured grid is still the best method if a wide range of spatial scales is involved, allowing us more easy adaptive strategies than those necessary in the structured case (e.g. Reference [13]). The IB technique was also adopted by other authors (e.g. see Reference [14]) in computations of complex geometry defined on a Cartesian grid. However, in such simulations, the interpolation problem is the main issue to be solved, as no deformation and no stresses are induced in the flow by the fixed body. The main problem is that no-slip and non-permeable conditions are required on the boundaries and the fulfillment of the continuity constraint, when the boundaries do not match the grid, is still an open issue.

As the diastole is characterized by a rapid time variation of the physiological variables, being the characteristic period less than half-second, a contribution of this study was also in applying a high order integration method, originally developed for the Finite Volumes (FV) approach on both structured and unstructured grids [15–18]. An approximate projection method, developed in the framework of the Fractional Time-Step (FTS) method [19, 20], is adopted; it is out of the aims of this paper to analyse the issue of the actual accuracy of the FTS method (e.g., see References [21–24]) but it is worthwhile observing the existence of convergence proofs [25] for the discrete formulation. Moreover, the actual accuracy of the IB method is still under investigation [12, 26, 27].

The outline of the paper follows: in Section 2 an analysis of both model limitations and validity of some simplifying hypotheses, is presented while mathematical and numerical techniques are described in Sections 3 and 4. In the last section, some results are presented and

compared to available experimental measurements, demonstrating that the main characteristic of diastole can be satisfactory represented [28, 29], albeit the simplicity of the adopted model.

2. DESCRIPTION AND MODELLING OF DIASTOLE; COMPUTATIONAL HYPOTHESES

The diastole is that part of the cardiac cycle during which the blood, flowing from the left atrium throughout the orifice of the mitral valve, fills the left ventricle. In order to quantify the diastolic performance of the left ventricle, the ventricular filling is often analysed by means of non-invasive Doppler measurements (an example of experimental measurement is reported in the plot of the pulsed Doppler of Figure 1(a) along with that one, obtained by means of trans-thoracic echo-cardiographs M-colour technique, reported in Figure 1(b).

Since the aortic valve closes until the opening of the mitral leaflets, the left ventricle practically results a closed chamber with constant volume. The myocardial relaxation, caused by complex physics and chemical mechanisms [30] not considered in the present paper, starts in the final part of the systole and it is characterized by a rapid exponential falling of the intra-ventricular pressure that prepares to the diastole. The gradient, generated by this sudden pressure drop, accelerates the blood from the left atrium towards the left ventricle, resulting in a rapid filling that can be observed in the latter plot of Figure 1(a), from the appearance of the so-called E-wave recorded from Doppler measurement. In normal conditions, mainly two factors contribute to originate the pressure gradient and the ventricular filling: the dynamic of the ventricular relaxation and the asymptotic pressures value in the left atrium. During the filling, depending on the elastic properties of the ventricle (i.e., the compliance), the left ventricular pressure increases; as a consequence, the pressure gradient decreases and, transiently, reverses. In the mid-portion of diastole (slow filling), only a small quantity of blood fills the ventricle, as it can be deduced from the flat part of the curve in Figure 1(a). Eventually, the atrial contraction increases the pressure value in the atrium, late in the diastole, by causing the blood to flow again in the left ventricle (A-wave) until the closure of the mitral valve. A normal time period of diastole is supposed to be about 0.5–0.6 s. During the filling, interacting the mitral leaflets with the fluid, they will become responsible of the production of vortical structures. Although in a normal function the turbulence level is not very high, because red blood cells could be destroyed by a strong microcirculation, the vorticity plays an important role into the closure of the valve, generating the re-circulation behind the leaflets. The closure of the leaflets can be altered by stenosis causing blood regurgitation in the atrium and these are some of the motivations that lead us to perform numerical simulations in order to support the implant of prosthetic valves.

From this general picture, it appears that the velocity patterns are not sufficient by themselves to provide a correct analysis of the diastolic performance and, in some cases, non-univocal interpretations are possible [1–4, 28, 29].

In light of such addressed physical description of the diastolic phase, some simplifying hypotheses are introduced into the numerical model. The main simplification consists of adopting a 2-D geometry, which clearly represents only a rough assumption of the real geometry while a fully 3-D case should be considered. However, as reported in References [6, 7, 9, 12], the plane of calculation can be physically assumed as the one bisecting the leaflets of the mitral valve, the root of the aorta and passing through the apex of the heart, as it is drawn in

Figure 2. On the boundary of this plane, only two inflows, representing the pulmonary veins (instead of the four present in the human heart), are assumed on the opposite faces of the atrium. The atrial contraction is modelled by assuming a suitable normal velocity distribution along the walls. More precisely, the time-dependent flow rate, measured in the pulmonary veins by means of the pulsed Doppler (see Figure 1(a)), is adopted as numerical inflow condition. It is quite complicated to extract useful numerical conditions from volume measurement during atrial contraction, because the volume variation rate does not directly define a normal velocity component along the atrial walls. Several normal velocity distributions were tested and the best results were obtained with the one presented in this paper; in particular, the normal velocity is assumed to be uniformly distributed along the walls and modulated in

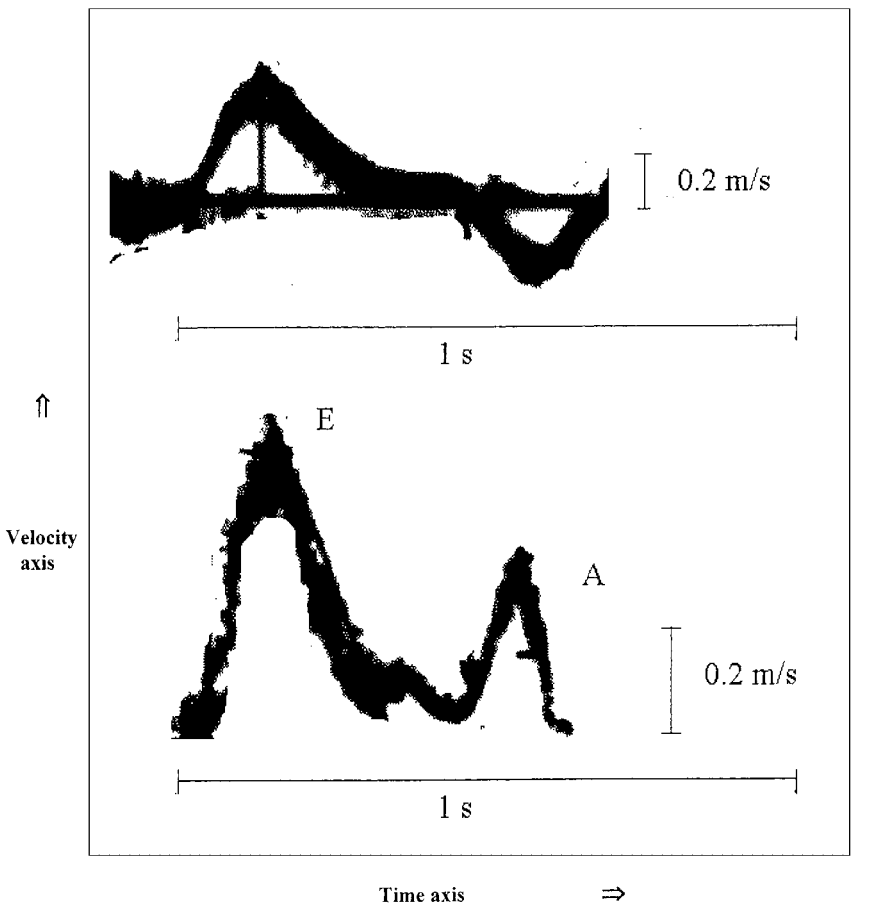

Figure 1. (a) Example of transmitral velocity measurement, during a normal left ventricle filling, as registered by the pulsed Doppler. The upper plot is representative of the recorded pulmonary flow, the lower one, with the characteristic E-A waves, of the transmitral flow. (b) Example of velocity map reconstructed by means of the velocity measurement with M-mode colour Doppler, during a normal left ventricle filling. The time is represented along the x-direction whilst, from bottom to top of the figure, the stream-wise velocity magnitude between the atrium and the ventricle is shown.

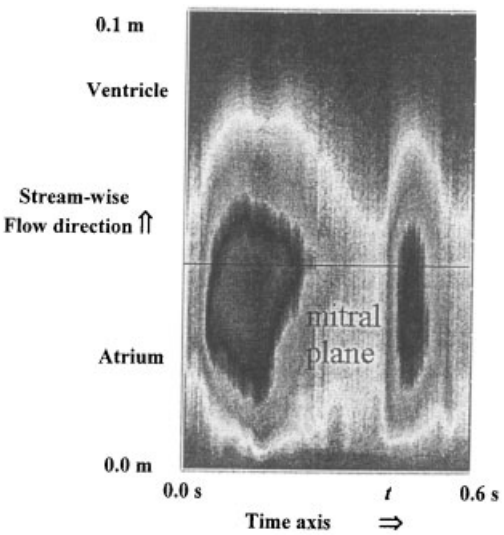

Figure 1. *Continued.*

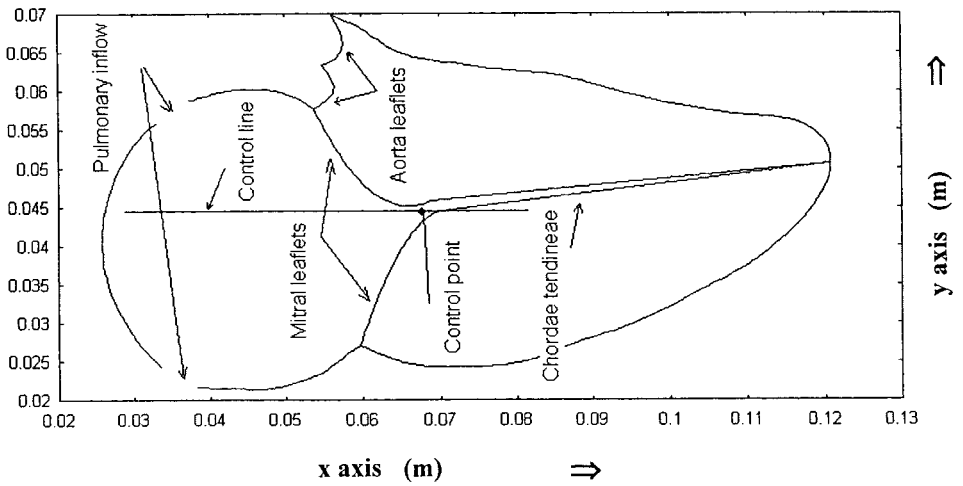

Figure 2. Sketch of the 2-D heart section adopted as computational domain. The line along which the velocities are registered is shown.

time by starting from the time of the beginning of the contraction, say T_{ac} during which the pulmonary flow reverses.

A further simplification is that no deformation of the ventricular boundary is considered thus, in order to satisfy the mass balance, blood is allowed to flow through the ventricular wall just as if the surfaces were permeable. For what it concerns the valve model, the mitral leaflets are assumed to be mass-less and the presence of the *chordae tendineae* has no influence on

the flow, apart from the forces they apply on the tips of the mitral leaflets. Finally, the leaflets are able to produce only normal stresses (i.e. directed along the local tangential direction of the material line).

A final comment concerns the quantitative comparison between experimental measurements and 2-D numerical computations. In the former case, Doppler technique measures fluid displacement for volume unit, while in the latter the 2-D variables are computed for unit of area thus an arbitrary scale representation is introduced. Although 2-D results cannot be considered fully explicative of real 3-D flows, good qualitative comparisons with experimental data are presented.

3. GOVERNING EQUATIONS AND MATHEMATICAL DESCRIPTION OF THE IMMERSED BOUNDARY METHOD

The blood motion is governed by the NS equations for incompressible flows constituted by the momentum equation, written in integral form in a generic domain Ω

$$\int_{\Omega} \frac{\partial \mathbf{v}}{\partial t} \, \mathrm{d}V = \int_{\partial\Omega} \mathbf{n}\cdot\mathbf{F} \, \mathrm{d}S \tag{1}$$

along with the continuity constraint

$$\int_{\partial\Omega} \mathbf{n}\cdot\mathbf{v} \, \mathrm{d}S = 0 \tag{2}$$

and proper initial and boundary conditions. In Equations (1) and (2), $\partial\Omega$ is the boundary of the domain, $\mathbf{v} = \mathbf{i}u + \mathbf{j}v$ is the velocity vector expressed in a Cartesian reference system ($\mathbf{x} = \mathbf{i}x + \mathbf{j}y$), the flux function $\mathbf{F}$ being expressed by the tensor

$$\mathbf{F} = -\mathbf{v}\mathbf{v} - \frac{\mathbf{I}p}{\rho} + v\underline{\nabla}\mathbf{v} + \frac{\mathbf{T}}{\rho} \tag{3}$$

Here, ρ is the blood density assumed constant (1.05×10^3 Kg m^{-3}), $v = \mu/\rho$ is the constant kinematics viscosity (6×10^{-3} m^2 s^{-1}), p is the pressure, $\mathbf{I}$ is the unit matrix and $\mathbf{T}$ is the stress tensor, including the contribution of the elastic forces due to the mitral leaflets. The mitral leaflets are considered as part of the fluid wherein additional stresses, produced by fibre strain, are transmitted to the rest of the fluid. In considering such an approach, the main advantage is that the equations, governing the flow motion, can be solved on a fixed domain (Eulerian description) while the motion of the leaflets can be simulated by that of an elastic chain of discrete points (Lagrangian description), moving into the domain and interacting with the fluid. The displacement of the material points along the fibre S is subject to the governing equation:

$$\frac{\partial \mathbf{X}(s,t)}{\partial t} = \mathbf{v}[\mathbf{X}(s,t),t] \tag{4}$$

(let us adopt the notation $\mathbf{X}(s,t) = (X(s,t), Y(s,t))$, $s \in S$, according to References [6–12]) fulfilling the condition that the leaflet points move at the local fluid velocity according to the no-slip condition. In particular, one velocity field $\mathbf{v}$, satisfying the constraint of Equation (2), can be used to describe simultaneously both the fluid and the fibre motion.

After introducing a simplified assumption, the leaflets are considered capable of exercising only tension (or compression) stresses. The leaflet stress, induced at any time t by the different motion of each discrete point, is $\sigma = \sigma[\varepsilon(\mathbf{X})]$ where σ is the tension acting along the elastic leaflet and $\varepsilon = \|\partial\mathbf{X}/\partial s\|$ is the strain rate. Therefore, in a local curvilinear reference system (s, n), such that the unit vector $\mathbf{i}_s$ is directed along the length of each associated leaflet element and $\mathbf{i}_n$ is normal to it, the only non-vanishing component of the (2×2) tensor $\mathbf{S}[\mathbf{X}(s,t)]$ is the element $S_{11} = \sigma$ thus one gets $\mathbf{S} = \sigma\mathbf{i}_s\mathbf{i}_s$. For each fibre-point, according to the Hooke's law, the stresses can be computed with respect to their initial length at rest as $\sigma = E\varepsilon$ and E is the given stiffness of the mitral leaflets. The stress vector associated to the direction $\mathbf{i}_s$ i.e., $\boldsymbol{\sigma} = \mathbf{i}_s \cdot \mathbf{S} = \mathbf{i}_s\sigma$, will generally produce in the global reference system both x- and y-components according to $\boldsymbol{\sigma} = \sigma(s_x\mathbf{i} + s_y\mathbf{j})$, wherein (s_x, s_y) are the components of the unit vector $\mathbf{i}_s$ along the directions $\mathbf{i}$ and $\mathbf{j}$, respectively. The equations describing the leaflet stresses are computed in the Lagrangian reference system so that, in order to compute the contribution in the Eulerian one, it is necessary to specify a functional relation between the two systems.

Then, a definition of a proper functional relation is required to correlate: $\int_{\partial\Omega} \mathbf{n}\cdot\mathbf{T}(\mathbf{x},t)\,\mathrm{d}S$ in Equation (1) to the elastic *force density*[‡] $\mathbf{f} = \partial(\mathbf{i}_s\sigma)/\partial s$, acting along the chain of points, in such a way that $\int_{\{s:\mathbf{X}(s,t)\subset\Omega\}} \mathbf{f}(s,t)\,\mathrm{d}s$ represents the total elastic force acting on the fluid contained in Ω. A relation of the kind $\sigma(\mathbf{x}) = M\sigma(\mathbf{X}), \forall\mathbf{x}\in\Omega$ accomplishes this goal, wherein M is a suitable operator defining the mapping between the Lagrangian and the Eulerian system. In this work the operator M will be expressed by means of a cosine-hill function, centred in $\mathbf{x}$ and having an influence radius that depends on a characteristic length of the grid, as it will be described more in details in the next section.

In many applications of the IB method, a 2-D Dirac function $\delta(\mathbf{x} - \mathbf{X}(s,t))$, expressed in a proper discrete form [6–12], is used; accordingly, it can be shown that Equation (4) becomes expressed as

$$\frac{\partial\mathbf{X}(s,t)}{\partial t} = \int_{\Omega} \mathbf{v}(\mathbf{x},t)\delta(\mathbf{x} - \mathbf{X}(s,t))\,\mathrm{d}V$$

as well as one has $\underline{\nabla}\cdot\mathbf{T}(\mathbf{x},t) = \int_S \cdot\mathbf{f}\,(s,t)\delta(\mathbf{x} - \mathbf{X}(s,t))\,\mathrm{d}s$.

In the approach proposed in References [6–12] the latter term has a singularity of the same type of the one-dimensional delta counterpart as a point-wise differential formulation is adopted. Owing to the integral formulation of Equation (1) used in the present paper, such a singularity disappears when $\underline{\nabla}\cdot\mathbf{T}$ is integrated over the sub-region corresponding to a Finite Volume.

4. DOMAIN DISCRETIZATION AND NUMERICAL PROCEDURE

The goal of obtaining accurate numerical solutions, by means of the IB technique, requires a careful consideration both of the numerical scheme and the domain discretization, as it is known that such a method is only first order accurate in space, close to the immersed material line. In fact, the lack of accuracy, coupled with the approximate resolution of continuity

[‡]The force balance on 1-D material fibre is, $\mathrm{d}/\mathrm{d}t \int_{s_1\leqslant s\leqslant s_2} m(s)[(\partial)/(\partial t)]\mathbf{X}(s,t)\,\mathrm{d}s = (\sigma\mathbf{i}_s)|_{s_1}^{s_2} + \int_{s_1\leqslant s\leqslant s_2} [-\mathbf{f}(s,t)]\,\mathrm{d}s$ where $-\mathbf{f}$ is the reaction of the fluid on the fibre. As the leaflet is assumed to be mass-less one gets $\mathbf{0} = \int_{s_1\leqslant s\leqslant s_2} [(\partial(\sigma\mathbf{i}_s))/(\partial s) - \mathbf{f}(s,t)]\,\mathrm{d}s$.

equation near the immersed boundary, creates mass conservation problems [9]. A proposed solution consists of refining the grid near the immersed lines and, following such approach, successful results were obtained [12]. Moreover, peak velocities of about $1\,\mathrm{m\,s^{-1}}$ are common during a normal diastole and the physiological Reynolds number can locally result in a magnitude order greater than 5×10^3. It turns out that the characteristic length and time scales are so small to require an accurate time-space numerical integration over a well-refined computational grid. The next subsections contain the details of both the domain and the equations system discretizations.

4.1. Unstructured-based domain discretization

To the authors' knowledge, the IB method simulations were originally performed using a non-physiological Reynolds number; in the simulations of Peskin *et al.* [6–12] the Reynolds number was kept 25 times smaller than the real one. Moreover, Stokes flows were considered in the second order *Immersed Interface Method* [26]. As the boundary layer thickness develops along the leaflets according to $\delta\approx\sqrt{\nu t}$, a grid step size of about 10^{-3} m should be adopted in this region in order to capture the features of the transitional flow. This is expected in the ventricular chamber, due to the massive flow separation induced by the boundary layers along the mitral leaflets.

In our opinion, in order to face such requirements, the type of domain discretization that is generally more suitable for both complex geometry and viscous flows, is the one based on a triangulation of the domain [13], allowing us a local refinement of the grid in a flexible way. In this study, the domain decomposition is performed by using a Frontal–Delaunay unstructured grid generator with post-optimization [11, 15]. The post-optimization procedure guarantees the presence of only five, six, or seven connected edges for each grid point, minimizing the interpolation errors. Although such a grid could allow us to consider the mitral leaflets as part of the boundaries and to adopt a moving adaptive grid, in order to use a fully Eulerian formulation [31], this procedure is computationally expensive and it introduces further approximations in the step-by-step grid adaptation and mesh-to-mesh interpolation procedure.

Some examples of the quality of the above referenced unstructured grid are shown in Figure 3. In Figure 3(a), the triangulation of the 2-D heart section, including a grid refinement near the walls, was obtained with only 1627 nodes. The markers in the figure represent an example of the mitral leaflet discretization at the initial resting condition of diastole. It is worthwhile highlighting that, although only a few nodes are used, the smallest grid size is about 4.4×10^{-4} m, which is 80 times smaller than the normal diameter of the mitral annulus and this grid size is sufficiently small to describe the boundary layers. Figure 3(b) shows the local refinement that is performed in the region influenced by the immersed lines and in Figure 3(c) the resulting angle distribution of the grid in Figure 3(b) is shown. The quality of the grid is associated with the interpolation errors that are minimized in the case of approximate equilateral triangles, as it is obtained in the present grid. Introducing a decomposition of the domain in K^T triangles, a dual tessellation D in N Finite Volumes Ω_i (see Figure 4) of the domain Ω is defined so that it is $\{\Omega_i\}:\Omega=\bigcup_{i=1}^{N}\Omega_i;\ \Omega_i\cap\Omega_j=\{0\}\ \forall i\neq j$, over which the NS Equations (1) and (2) are solved.

Furthermore, the l-th side of the finite volume is obtained by linking the geometrical centres (P and Q) of two adjacent triangles as it is shown in Figure 4. Thus, the flux section is not automatically perpendicular to the common side of such triangles and a proper projection must be performed in the flux computation.

4.2. The Fractional Time-Step-based numerical procedure: flux reconstruction and mapping function on unstructured grid

The numerical integration procedure is based on the *Fractional Time-Step* (FTS) Method [19–24] applied into the framework of a Finite Volume approach originally developed on both structured and unstructured grids, for simulating high Reynolds numbers flows and reported

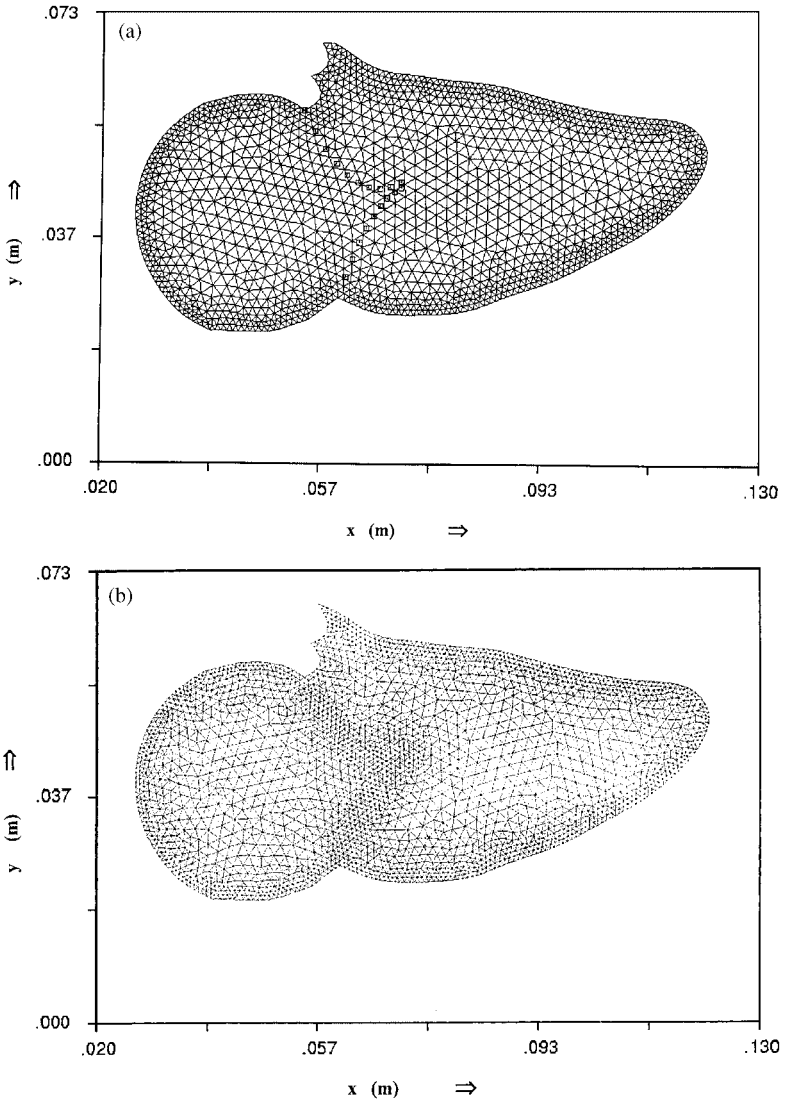

Figure 3. (a) Example of unstructured grid generation for the computational domain showed in Figure 2 with a local refinement on the walls. The total points number is 1627 and the obtained smallest grid size is $\approx 4.4 \times 10^{-4}$ m. (b) The same grid of (a) with a local refinement in the region influenced by the immersed lines. (c) Angles distribution of the grid in (b); the values, expressed in degrees, are reported in the x-direction while the number of angles, in the y-direction.

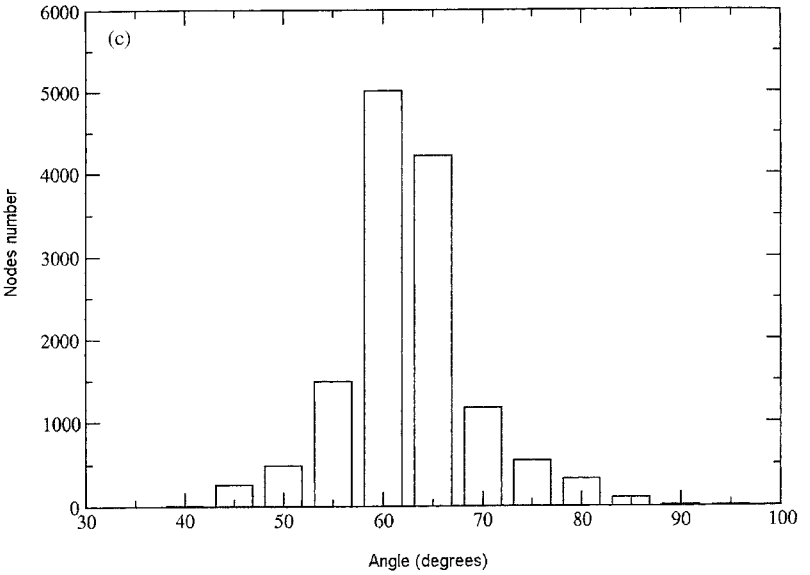

Figure 3. *Continued.*

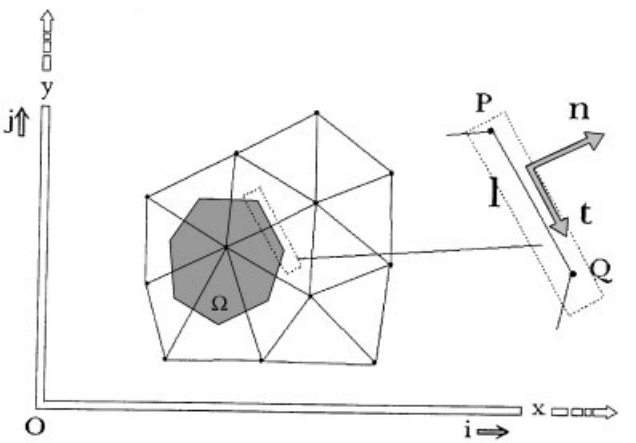

Figure 4. Geometrical definition of the Finite Volume Ω_i adopted on the 2-D unstructured grid and details of a generic l-th flow section $\partial\Omega_i$, along which the polynomials are integrated, is also reported.

in detail in References [15–18, 32–34]. The N momentum equations, associated with the continuity constraint of Equation (2), can be written in a weak formulation according to Equation (1), as:

$$[\bar{\mathbf{v}}(\mathbf{x}_i, t^{n+1}) - \bar{\mathbf{v}}(\mathbf{x}_i, t^n)] \equiv \frac{1}{|\Omega_i|} \int_{\Omega_i} [\mathbf{v}(\mathbf{x}', t^{n+1}) - \mathbf{v}(\mathbf{x}', t^n)] \, \mathrm{d}\mathbf{x}'$$
$$= \frac{1}{|\Omega_i|} \int_{t^n}^{t^{n+1}} \mathrm{d}t \int_{\partial\Omega_i} \mathbf{n}\cdot\mathbf{F} \, \mathrm{d}S \tag{5}$$

where $\mathbf{x}_i$ is a point in Ω_i, $|\Omega_i|$ is the measure of the i-th FV and $\bar{\mathbf{v}}$ is the local cell-averaged velocity.

The adopted methodology takes into account the requirement of solving flow fields having significant contributions coming from the highest wavenumbers components in the resolved spectrum $(0, K_c)$, being $K_c = \pi/h$ the highest theoretically resolvable wavenumber, in the 1-D counterpart, given a grid of size h and a spectral method. In fact, while these components result exactly resolved by means of spectral methods, the volume average smoothes the higher components of the resolved spectrum (the wavenumber components are affected since before the second half of the spectrum) and a deconvolution procedure, developed for the FV scheme on unstructured grid, is adopted as described in the following subsections.

4.2.1. Flux reconstruction methodology on unstructured grid. The velocity functional representation, in each sub-domain Ω_i, is obtained by means of a localized Taylor expansion about the point $\mathbf{x}_i$:

$$\begin{aligned} \bar{\mathbf{v}}(\mathbf{x}_i) &= \frac{1}{|\Omega_i|} \sum_{l=0}^{m} \frac{1}{l!} \int_{\Omega_i} P^l \mathbf{v}(\mathbf{x}') \, \mathrm{d}\mathbf{x}' + O(|\Delta \mathbf{x}_i'|^{m+1}) \\ P^l \mathbf{v}(\mathbf{x}') &\equiv \left[(x' - x_i) \frac{\partial}{\partial x'} \bigg|_{\mathbf{x}' = \mathbf{x}_i} + (y' - y_i) \frac{\partial}{\partial y'} \bigg|_{\mathbf{x}' = \mathbf{x}_i} \right]^{(l)} \mathbf{v} \end{aligned} \tag{6}$$

wherein the operator P^l, expressing the symbolic power of the differential operators, is obtained by taking the l-th power and replacing each product of l partial derivatives by the l-th derivative with respect to corresponding variable [16]. Thus, when Equation (6) is truncated at the order $m+1$, the LHS of Equation (5) can be rewritten in a compact form as:

$$[\bar{\mathbf{v}}(\mathbf{x}_i, t^{n+1}) - \bar{\mathbf{v}}(\mathbf{x}_i, t^n)] \equiv \Delta_t \bar{\mathbf{v}}^{n+1}(\mathbf{x}_i) \cong (I_{\mathbf{x}_i} - R^{(m)}_{\mathbf{x}_i}) \Delta_t \mathbf{v}^{n+1} \tag{7}$$

where $I_{\mathbf{x}_i}$ is the identity operator in $\mathbf{x}_i$ and $R^{(m)}_{\mathbf{x}_i}$ is a linear differential operator defined as:

$$R^{(m)}_{\mathbf{x}_i} \mathbf{v} \equiv - \frac{1}{|\Omega_i|} \sum_{l=1}^{m} \frac{1}{l!} \int_{\Omega_i} P^l \mathbf{v}(\mathbf{x}') \, \mathrm{d}\mathbf{x}' \tag{8}$$

Under suitable hypotheses [35], it is possible to do the approximate inversion of the operator $(I_{\mathbf{x}} - R^{(m)}_{\mathbf{x}})$ according to the following expansion

$$(I_{\mathbf{x}} - R^{(m)}_{\mathbf{x}})^{-1} = I_{\mathbf{x}} + R^{(m)}_{\mathbf{x}} + (R^{(m)}_{\mathbf{x}})^{(2)} + \cdots \tag{9}$$

that will be truncated to the m-th power of the associate diameter $2r$, being $|\Omega_i| = \pi r^2$.

The effect of this operator can be better explained by considering the counterpart in the 1-D Fourier space: a resolved component e^{ikx} is drastically smoothed close to the cut-off frequency K_c by the volume integral adopted in Equation (5), which consists in a *top-hat* filtering operation. For example, the convolution product $\overline{e^{ikx}} = 1/2h \int_{x-h}^{x+h} e^{ikx'} \, \mathrm{d}x'$ can be expressed in the Fourier space as $G(k) e^{ikx}$, where $G(k) = \sin(kh)/kh$ is the transfer function associated to the top-hat filtering. Around the cut-off frequency, some information is recovered by means of the de-filtering operation of Equation (9) and they contribute to reconstruct a more accurate (with respect to the real one $\bar{\mathbf{v}}$) averaged variable, say $\tilde{\mathbf{v}}$, than the previous $\bar{\mathbf{v}}$. In fact, according to the Fourier transform of Equation (9), the modified transfer function $H(k)$ is expressed

as $H(k)=(C_0 + C_1 kh + C_2(kh)^2 + \cdots)G(k)$, C_i being the coefficients of the moments of the Taylor series. The highest resolved frequencies are, therefore, better represented [32, 33] and Equation (5) represents a new balance equation for such de-filtered velocity. The main consequence of this modification is that one has a resolved field that tends to be similar to that one obtained from a spectral method, according to an increasing order m. The final comment is that a proper closure should take into account the contribution of the residual fluctuation of $\mathbf{v}$ with respect to $\tilde{\mathbf{v}}$. This issue is more properly addressed in the framework of the 3-D Large Eddy Simulation of turbulent flow and is not considered in this paper. Thus, no sub-grid scale models are considered in this work and the direct approximation $\mathbf{F}(\mathbf{v}) \cong \mathbf{F}(\tilde{\mathbf{v}}) \equiv \tilde{\mathbf{F}}$ is adopted. Owing to the de-filtering operation, this approximation is more accurate than the one represented by $\mathbf{F}(\mathbf{v}) \cong \mathbf{F}(\bar{\mathbf{v}})$ and one can find that the modified equation can be reinterpreted as an equation with an implicit sub-grid scale model [33]. In conclusion, Equation (5) approximates as:

$$\Delta_t \tilde{\mathbf{v}}^{n+1}(\mathbf{x}_i) \cong \frac{1}{|\Omega_i|} \int_{t^n}^{t^{n+1}} \mathrm{d}t \int_{\partial\Omega_i(\mathbf{x})} \mathbf{n}\cdot(I_{\mathbf{x}'} + R^{(m)}_{\mathbf{x}'} + \cdots)\tilde{\mathbf{F}}\,\mathrm{d}S \tag{10}$$

Some fundamental differences arise by applying the same de-filtering approach on structured or unstructured grids, because the commutation property between line integrals and derivatives does not apply on an unstructured grid, as well as on non-uniform structured grids. While in Equation (5) this property is not required, Equation (10) results by disregarding the commutation terms coming from the application of Equation (9) on $\Omega(\mathbf{x})$ and, as a consequence,[§] $m=1$ is the congruent order of the expansion of Equation (8) to be adopted. Only on uniform structured grids the derivatives and the integrals do commute and the integral terms in $R^{(1)}_{\mathbf{x}}$ vanish if $\mathbf{x}_i$ is the geometric centre $\mathbf{x}_g$ of the Finite Volume, according to the second order approximation $\bar{\mathbf{v}}(\mathbf{x}_g)=\mathbf{v}(\mathbf{x}_g)+O(h^2)$. Conversely, on the adopted unstructured grid, it generally results $\mathbf{x}_i \neq \mathbf{x}_g$ and, in order to retain second order accuracy, the integrals of the linear terms in Equation (10) must be computed while a higher order of accuracy cannot be reached without taking into account the commutation error.

All of the integral terms appearing in Equation (9) can be computed by simply adopting, over each triangle T_j composing Ω_i and having its vertices in the points i, n, p (n, p are the centre of two adjacent triangles), a local system of co-ordinates

$$\begin{aligned} x' &= \xi_i x_i + \xi_n x_n + \xi_p x_p \\ y' &= \xi_i y_i + \xi_n y_n + \xi_p y_p \end{aligned} \tag{11}$$

being ξ_i, ξ_n, ξ_p the shape functions in a Finite Element fashion. Accordingly, in Equation (9) the integrals to be computed are the following:

$$\frac{1}{|\Omega_i|}\int_{\Omega_i}(x'-x_i)\,\mathrm{d}V = x_g - x_i; \quad \frac{1}{|\Omega_i|}\int_{\Omega_i}(y'-y_i)\,\mathrm{d}V = y_g - y_i$$

[§]Considering the rule of derivation of an integral function, Equation (5) should be correctly written taking into account that for smooth grids: $(I_{\mathbf{x}} + R^{(m)}_{\mathbf{x}} + \cdots)\{[1/|\Omega_i(\mathbf{x})|]\int_{\partial\Omega_i(\mathbf{x})}\mathbf{n}\cdot\tilde{\mathbf{F}}\,\mathrm{d}S\} = [1/|\Omega_i(\mathbf{x})|]\int_{\partial\Omega_i(\mathbf{x})}\mathbf{n}\cdot(I_{\mathbf{x}} + R^{(m)}_{\mathbf{x}} + \cdots)\tilde{\mathbf{F}}\,\mathrm{d}S + O[R^{(m)}_{\mathbf{x}}\partial\Omega_i(\mathbf{x}), R^{(m)}_{\mathbf{x}}[1/|\Omega_i(\mathbf{x})|]]$.

$$\frac{1}{|\Omega_i|}\int_{\Omega_i}(x'-x_i)(y'-y_i)\,\mathrm{d}V = x_i y_i - x_i y_g - x_g y_i + \frac{1}{|\Omega_i|}\int_{\Omega_i} x'y'\,\mathrm{d}V$$
$$\frac{1}{|\Omega_i|}\int_{\Omega_i}(x'-x_i)^2\,\mathrm{d}V = x_g^2 - 2x_g x_i + \frac{1}{|\Omega_i|}\int_{\Omega_i} x'^2\,\mathrm{d}V$$
$$\frac{1}{|\Omega_i|}\int_{\Omega_i}(y'-y_i)^2\,\mathrm{d}V = y_g^2 - 2y_g y_i + \frac{1}{|\Omega_i|}\int_{\Omega_i} y'^2\,\mathrm{d}V$$
$$\cdots \tag{12}$$

and so on for higher values of m. Those of the integrals of Equation (12) required for the inversion of Equation (9) are computed by substituting Equation (11) and by considering that:

$$\int_{T_i} \xi_i^{\alpha}\xi_\eta^{\beta}\xi_p^{\gamma}\,\mathrm{d}V = \frac{\alpha!\beta!\gamma!}{(\alpha+\beta+\gamma+2)!}2|T_j| \tag{13}$$

being $|T_j|$ the measure of the j-th triangle extension.

4.2.2. Leaflet stresses calculation by means of the mapping method. In order to compute the stress tensor $\mathbf{T}(\mathbf{x},t)$, the equations that provide the contribution of the leaflet stresses in the Lagrangian system, must be firstly solved; thus, by using N_l one-dimensional elements, for which a linear behaviour for the nodal displacement is assumed, each leaflet is discretized. The stresses distribution could be computed from the known configuration $\mathbf{X}^n$ i.e., the configuration of the immersed lines at the beginning of the $(n+1)$-th time step. The updated position $\mathbf{X}^{n+1}$ is computable, from the Eulerian variables,[‖] by integrating Equation (4) according to $\mathbf{X}(s,t^{n+1}) = \mathbf{X}(s,t^n) + \Delta t\mathbf{v}[\mathbf{X}(s,t^n)] + \Delta t^2\mathbf{a}[\mathbf{X}(s,t^n)]/2 + O(\Delta t^3)$ being $\mathbf{a}[\mathbf{X}(s,t^n)]$ the Lagrangian acceleration. As it is known that some stiffness problems could arise, this kind of *explicit* second order integration requires care in adopting a proper time integration step, owing to restricted stability region constraints. Some authors [6–12] suggest getting the solution of the fluid-boundary interaction equations by computing a preliminary configuration $\mathbf{X}^*$ approximating $\mathbf{X}(s,t^{n+1})$ (the so-called *approximately implicit* IB method), then compute the elastic force distribution from such configuration.

In the computations presented in this paper, such an approach was adopted since it results sufficiently stable for our aims and much less computationally onerous than a fully implicit one. The configuration $\mathbf{X}^*$, along with the stresses $\mathbf{S}$ depending on the resulting fibre strain, is computed from a second order accurate prediction–correction step. As each element expresses a stress matrix in the local reference system, by assembling the global stress matrix in a Finite Element fashion, the stresses on the $2(N_l+1)$ nodes (always in the Lagrangian reference system) are computed; finally they are mapped back into the Eulerian system by means of a spreading operator. The updated configuration $\mathbf{X}(s,t^{n+1})$ will be obtained after the projection step that will allow us to compute the divergence-free velocity. This procedure will guarantee that leaflet equilibrium and fluid conservation principles are satisfied at t^{n+1} congruently to the accuracy of the global method.

[‖]By remembering that any vector $\mathbf{b}$ expressed in the Lagrangian system is related to that on the Eulerian one from $\mathbf{b}[\mathbf{X}(s,t)] = \int_\Omega \mathbf{b}(\mathbf{x},t)\delta(\mathbf{x}-\mathbf{X}(s,t))\,\mathrm{d}V$, i.e. by a proper interpolation of the set $\{\mathbf{b}_i\}$.

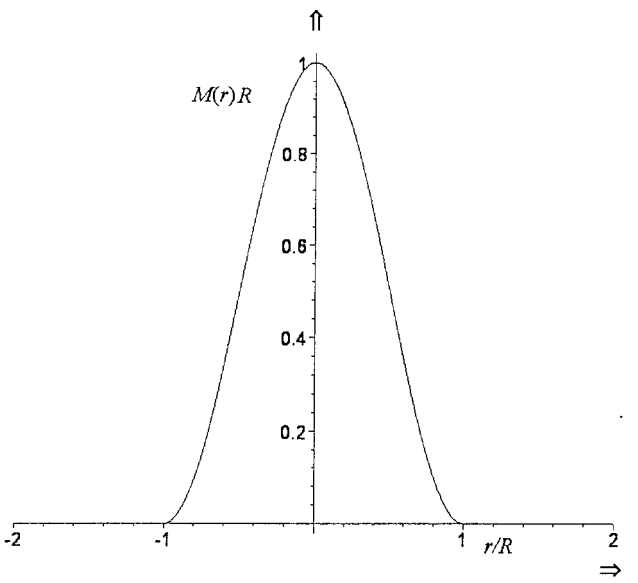

Figure 5. Mapping function $M(r)R$, spreading the stresses onto the Eulerian grid, versus the local radius r.

For what it concerns the spreading of the stresses, by adopting for this purpose the Heavyside function ($H(x)=1$ for $x \geqslant 0$ and $H(x)=0$ elsewhere), the mapping operator M is represented by a cosine-hill function (see Figure 5):

$$M_i(r) = \frac{1}{2R_i}\left[H(R_i - r) - H(-R_i - r)\right]\left[1 + \cos\left(\frac{\pi r}{R_i}\right)\right] \tag{14}$$

centred in $\mathbf{x}_i$ and having a radius $R_i = 2\sqrt{|\Omega_i|/\pi}$, where $4|\Omega_i| = \pi R_i^2$ is the measure of the chosen local influence region. In this way, each sub-domain Ω_i results in being influenced by a local region directly related to its characteristic area because M_i varies in the domain according to the local refinement and, it is ensured that the mapping function covers all points forming Ω_i. The function M_i satisfies the following conditions:

$$\begin{aligned}
&\int_{-\infty}^{\infty} M_i(r)\,\mathrm{d}r = 1\\
&M_i(r) = 0 \quad \text{when } |r| \geqslant R_i\\
&M_i(r) = M_i(-r)\\
&M_i'(r) = -M_i(r)[\delta(R_i - r) - \delta(R_i + r)] - \frac{1}{2R_i^2}\sin\left(\frac{\pi r}{R_i}\right)\pi[H(R_i - r) - H(-R_i - r)]
\end{aligned} \tag{15}$$

the first three ensuring that M_i corresponds to a δ-distribution. This approach results in an agreement with the one analysed in Reference [12], where it is demonstrated that nested refinements, on a structured grid, reduce the local error close to the immersed interface.

Now, the relation between the total elastic force acting on the fluid contained in Ω_i and the stresses acting along the chain of points can be expressed. According to what was described in Section 3, $\mathbf{T}(\mathbf{x}_i,t)=\sum_k M_i(r_k)\mathbf{S}[\mathbf{X}(s_k,t)]$, $\forall\mathbf{x}_i$ accomplishes this goal; furthermore, by remembering the expression for the associated stress vector $\boldsymbol{\sigma}=\mathbf{i}_s\sigma=\sigma(s_x\mathbf{i}+s_y\mathbf{j})$, one gets the integral contribution in the FV as $\int_{\partial\Omega_i}\mathbf{n}\cdot\mathbf{T}\,\mathrm{d}S=\int_{\partial\Omega_i}\mathbf{n}\cdot M(\mathbf{i}_s\sigma\mathbf{i}_s)\,\mathrm{d}S=\int_{\partial\Omega_i}(\mathbf{n}\cdot\mathbf{i}_s)M[\sigma(s_x\mathbf{i}+s_y\mathbf{j})]\,\mathrm{d}S$. This way, it is evident that the explicit expression between the tensor $\mathbf{T}$ and the elastic force density according to $\int_{\partial\Omega_i}\mathbf{n}\cdot\mathbf{T}(\mathbf{x},t)\,\mathrm{d}S=\int_{\Omega_i}[\int_S\mathbf{f}(s,t)\delta(\mathbf{x}-\mathbf{X}(s,t))\,\mathrm{d}s]\,\mathrm{d}V$ as introduced in Section 3.

After having spread the stresses on the Eulerian mesh, the diffusive and convective integrals can be computed as illustrated in the following section.

4.2.3. Time integration and numerical algorithm. The first step of the FTS method consists of computing an intermediate velocity field, say $\tilde{\mathbf{v}}^*$, which is obtained by solving Equation (10) after disregarding the pressure contribution in Equation (3), namely by evaluating the approximate flux $\tilde{\mathbf{F}}^*=\mathbf{F}-\mathbf{I}p/\rho$. Accordingly, Equation (19) becomes:

$$\begin{aligned}\tilde{\mathbf{v}}^*(x_i,t^{n+1})-\tilde{\mathbf{v}}^*(x_i,t^n)&=\frac{1}{|\Omega_i|}\int_{t^n}^{t^{n+1}}\mathrm{d}t\int_{\partial\Omega_i(\mathbf{x})}\mathbf{n}\cdot(I_{\mathbf{x}'}+R^m_{\mathbf{x}'})\tilde{\mathbf{F}}^*\,\mathrm{d}S\\&\cong\frac{1}{|\Omega_i|}\sum_{l=1}^{b_i}\int_{\partial\Omega_{il}}\mathbf{n}_l\cdot\tilde{\mathbf{F}}_l^{*(k,m)}\,\mathrm{d}S_l\end{aligned}\tag{16}$$

where b_i is the number of edges composing the FV boundary i.e. $\bigcup_{l=1}^{b_i}\partial\Omega_{il}=\partial\Omega_i$, $\mathbf{n}_l$ is the outgoing unit vector normal to the l-th section $\partial\Omega_{il}$ (see Figure 4) and $\tilde{\mathbf{F}}_l^{*(k,m)}$ is the time integrated numerical flux function (see References [16, 18] for more details) given by

$$\tilde{\mathbf{F}}_l^{*(k,m)}=(I_{\mathbf{x}}+R^{(m)}_{\mathbf{x}})E_t^{(k)}\tilde{\mathbf{F}}_l^*\tag{17}$$

By defining $L_{ad}g=-\underline{\nabla}\cdot(\tilde{\mathbf{v}}^*g)$, the advective operator applied to a generic scalar function g, it results:

$$E_t^{(k)}g=\left[I+\frac{\Delta t}{2}L_{ad}+\cdots+\frac{\Delta t^{k-1}}{k!}L_{ad}^{(k-1)}\right]g\tag{18}$$

where $E_t^{(k)}$ is an operator taking into account a Lax–Wendroff-type single step time marching integration of the advective terms (see Reference [34]); in the following computations, the value $k=3$ is fixed. The line integrals in Equation (16) are rewritten as:

$$\sum_{l=1}^{b_i}\int_{\partial\Omega_{il}}\mathbf{n}_l\cdot\tilde{\mathbf{F}}_l^{*(k,m)}\,\mathrm{d}S=\sum_{l=1}^{b_i}\int_{P_l}^{Q_i}\mathbf{n}_l\cdot\tilde{\mathbf{F}}_l^{*(k,m)}\,\mathrm{d}S_l\tag{19}$$

where P_l and Q_l are the extreme points of a generic flux section l, as illustrated in Figure 4, over which it results:

$$\begin{aligned}\mathbf{n}&=n_x\mathbf{i}+n_y\mathbf{j};&\mathbf{t}&=t_x\mathbf{i}+t_y\mathbf{j}\\n_x&=\mathbf{i}\cdot\mathbf{n}=\cos(\widehat{\mathbf{in}});&t_x&=\mathbf{i}\cdot\mathbf{t}=\cos(\widehat{\mathbf{it}})\\n_y&=\mathbf{j}\cdot\mathbf{n}=\cos(\widehat{\mathbf{jn}});&t_y&=\mathbf{j}\cdot\mathbf{t}=\cos(\widehat{\mathbf{jt}})\\\mathbf{n}\cdot\tilde{\mathbf{v}}^*&=n_x\tilde{u}^*+n_y\tilde{v}^*;&\mathbf{n}\cdot\underline{\nabla}&=n_x\frac{\partial}{\partial x}+n_y\frac{\partial}{\partial y}\end{aligned}\tag{20}$$

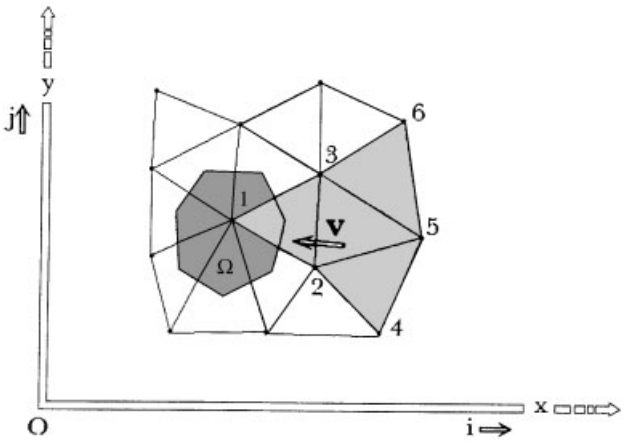

Figure 6. Geometrical definition of the 2-D upwind criterion adopted on the unstructured grid. The example shows the case $\mathbf{n}\cdot\mathbf{v}<0$ and $\mathbf{n}\cdot\mathbf{t}<0$. The region formed by the four triangles (1,2,3) –(2,4,5)–(3,5,6)–(2,5,3) is that adopted as support for defining the complete second-degree polynomial over the flow section $\partial\Omega_{il}$.

Then, by introducing a complete second degree 2-D polynomial given by

$$\tilde{\mathbf{v}}^*(x,y)=c_0+c_1x+\cdots+c_5y^2=|1,x,\ldots,y^2|\cdot|c_0,c_1,\ldots,c_5|^T=\mathbf{P}\cdot\mathbf{C}^T \tag{21}$$

whose support region depends on the velocity vector direction according to the multidimensional upwinding criterion illustrated in Figure 6, the flux $\tilde{\mathbf{F}}_l^*$ can be computed as a function of $\tilde{\mathbf{v}}^*$ and the advective and diffusive integrals can be expressed by means of the corresponding integrals of the monomial basis vector $\mathbf{P}$ as:

$$\begin{aligned}\sum_{l=1}^{b_i}\int_{P_l}^{Q_l}\mathbf{n}_l\cdot\tilde{\mathbf{F}}_l^{*(k,m)}\,\mathrm{d}S_l=&-\sum_{l=1}^{b_i}\frac{1}{t_{x_l}}\int_{x_{P_l}}^{x_{Q_l}}\mathbf{n}_l\cdot(I_{\mathbf{x}}+R_{\mathbf{x}}^{(m)})E_t^{(k)}[\tilde{\mathbf{v}}^*(x,y_l(x))\tilde{\mathbf{v}}^*(x,y_l(x))]\,\mathrm{d}x\\&+\nu\sum_{l=1}^{b_i}\frac{1}{t_{x_l}}\int_{x_{P_l}}^{x_{Q_l}}\mathbf{n}_l\cdot(I_{\mathbf{x}}+R_{\mathbf{x}}^{(m)})E_t^{(k)}\underline{\nabla}\tilde{\mathbf{v}}^*(x,y_l(x))\,\mathrm{d}x\\&+\frac{1}{\rho}\sum_{l=1}^{b_i}\frac{1}{t_{x_l}}\int_{x_{P_l}}^{x_{Q_l}}\mathbf{n}_l\cdot(I_{\mathbf{x}}+R_{\mathbf{x}}^{(m)})E_t^{(k)}\mathbf{T}(x,y_l(x))\,\mathrm{d}x\end{aligned} \tag{22}$$

where $\mathrm{d}S_l=\mathrm{d}x/t_{x_l}$ and the edge (P_lQ_l) is defined by the linear equation:

$$y_l(x)=\left(\frac{y_{Q_l}-y_{P_l}}{x_{Q_l}-x_{P_l}}\right)(x-x_{P_l})+y_{P_l}=a_l+b_lx \tag{23}$$

along which the polynomials in Equation (22) are integrated. Observe that $\mathbf{T}(x,y)$ is locally reconstructed, on the same support region used for the velocity field, by interpolating the nodal values $\mathbf{T}(\mathbf{x}_i)$ previously obtained from the mapping method.

If the initial condition at t^n is assigned fulfilling the mass balance constraint, then $\tilde{\mathbf{v}}^*(\mathbf{x}_i,t^n)=\tilde{\mathbf{v}}(\mathbf{x}_i,t^n)$ and one can assign $\tilde{\mathbf{F}}^*=\tilde{\mathbf{F}}^*[\tilde{\mathbf{v}}^*(\mathbf{x},t^n)]=\tilde{\mathbf{F}}^*[\tilde{\mathbf{v}}(\mathbf{x},t^n)]$ in the Equation (22); the intermediate velocity can be computed by adopting this explicit single-step time-marching

scheme:

$$\tilde{\mathbf{v}}^*(\mathbf{x}_i, t^{n+1}) = \tilde{\mathbf{v}}(\mathbf{x}_i, t^n) + \frac{\Delta t}{|\Omega_i|} \sum_{l=1}^{b_i} \int_{P_l}^{Q_l} \mathbf{n}_l \cdot \tilde{\mathbf{F}}_l^{*(k,m)} \, \mathrm{d}S_l \tag{24}$$

representing the prediction step of the FTS method.

4.3. The Fractional Time-Step-based numerical procedure: solution of the projection step

The projection step is based on the theoretical assumption that, if $\tilde{\mathbf{v}}^*$ is sufficiently smooth, according to the Helmholtz–Hodge decomposition in a bounded domain Ω, $\tilde{\mathbf{v}}^*$ can be decomposed as $\tilde{\mathbf{v}}^* = \tilde{\mathbf{v}} + \underline{\nabla}\varphi$, i.e. in the sum of a divergence-free vector and a pure gradient field. Thus, a projection operator P, extracting the divergence-free part of $\tilde{\mathbf{v}}^*$, is introduced [19, 36] and applied to both sides of Equation (10), in which Equation (24) is substituted, while taking into account that $P(\underline{\nabla} p) = \mathbf{0}$ and $P(\tilde{\mathbf{v}}) = \tilde{\mathbf{v}}$. If $\mathbf{n} \cdot \mathbf{v} = 0$ on $\partial\Omega$, then the components $(\tilde{\mathbf{v}}, \underline{\nabla}\varphi)$ are orthogonal and it can be shown that the decomposition is unique [36]; as a consequence, in order to retain the orthogonal decomposition when $\mathbf{n} \cdot \mathbf{v} = \mathbf{v}_n \neq 0$ on $\partial\Omega$, one must consider $\varphi = \varphi' + f$ where f is a suitable harmonic function such that $\mathbf{n} \cdot \underline{\nabla} f = -v_n$ on $\partial\Omega$ so that the orthogonal components become $(\tilde{\mathbf{v}} + \underline{\nabla} f, \underline{\nabla}\varphi')$; similar considerations apply for the Helmholtz–Hodge decomposition with assigned tangential component.

In order to ensure a final divergence-free velocity field, the intermediate field of Equation (24) is corrected by means of the pressure contribution, corresponding to the potential part of the velocity $\tilde{\mathbf{v}}^*$. It is worthwhile to remark that for isothermal incompressible fluids no primitive pressure equation exists being the pressure p derived only from Equation (1) coupled with the constraint of Equation (2). The equation for the time-averaged pressure

$$\langle p \rangle(\mathbf{x}) = \frac{1}{\Delta t} \int_{t^n}^{t^{n+1}} p(\mathbf{x}, t) \, \mathrm{d}t \tag{25}$$

is obtained by performing the divergence of Equation (10), where the velocity field $\tilde{\mathbf{v}}(\mathbf{x}, t^{n+1})$ is imposed to be divergence-free. The result consists of

$$\int_{\partial\Omega_i} \frac{\partial \langle p \rangle}{\partial n} \, \mathrm{d}S = \frac{\rho}{\Delta t} \int_{\partial\Omega_i} \mathbf{n} \cdot [\tilde{\mathbf{v}}^*(\mathbf{x}, t^{n+1}) - \tilde{\mathbf{v}}(\mathbf{x}, t^n)] \, \mathrm{d}S \tag{26}$$

which is the Poisson equation** for $\langle p \rangle$.

It is well known [36] that Equation (26) admits a unique solution (apart from a constant) as long as the non-homogeneous Neumann boundary conditions

$$\frac{\Delta t}{\rho} \frac{\partial \langle p \rangle}{\partial n} = \mathbf{n} \cdot \tilde{\mathbf{v}}^*(\mathbf{x}, t^{n+1}) - v_n^{n+1}$$

associated with the whole boundary $\partial\Omega$ fulfil the compatibility condition (imposed the constraint of Equation (2)); this condition is also necessary for solving Equation (26) by means of iterative procedures, in this case is an optimized SOR. This kind of boundary condition

**Let us observe that the source term in Equation (26) contains also the residual velocity divergence of the time step n. This is done in order to avoid local divergence errors (due to approximate projection that depends on the local truncation error) to cumulate during time integration. However, its surface integral over $\partial\Omega$ must vanish.

accomplishes the fact that neither pressure nor intermediate velocity values are required on the boundary, but the only knowledge of the normal velocity v_n^{n+1} is required to close the problem. The final result expressed by Equation (26) and such boundary conditions consists of an equivalent Poisson problem with homogeneous Neumann boundary conditions and a modified source term, obtained when the divergence operator is defined onto the subspace of vectors with normal component on the boundary equal to the normal velocity component v_n^{n+1}, this equivalence does not imply that the computed pressure field has a vanishing normal derivative on the boundary.

Owing to the arbitrary pressure reference value, one can assign a value in a point and according to the Helmholtz–Hodge decomposition with tangential component $\mathbf{t}\cdot\underline{\nabla}\langle p\rangle$ assigned along the boundary ($\mathbf{t}$ is the unit tangential vector along $\partial\Omega$), the solution is still unique if the compatibility conditions are verified. Therefore, when tangential components are assigned, the normal velocity component cannot be prescribed but it must result from the interior solution. In the present computations, the reference pressure value is assigned at a point onto the ventricle walls and $\mathbf{t}\cdot\underline{\nabla}\langle p\rangle = 0$ allows us to assign the time behaviour of the pressure along that part of $\partial\Omega$ corresponding to the ventricular walls.

Eventually, the intermediate velocity field $\tilde{\mathbf{v}}^*(\mathbf{x}, t^{n+1})$ is projected onto the space of divergence-free vector fields and the single step time marching formula can be corrected by the pressure term as:

$$\tilde{\mathbf{v}}(\mathbf{x}_i, t^{n+1}) = \tilde{\mathbf{v}}^*(\mathbf{x}_i, t^{n+1}) - \frac{\Delta t}{\rho|\Omega_i|}\int_{\partial\Omega_i}\mathbf{n}\langle p\rangle\,\mathrm{d}S \tag{27}$$

Even if it is out of the aim of the present study to analyse the accuracy of the IB method, it is known that the FTS procedure can limit the time accuracy of the solution to be first order, albeit higher order schemes are adopted separately in the prediction and projection steps. It is still debated if the fractional method could be adopted for accurately computing in time both velocity and pressure [21–24]. This turns out because the splitting between the velocity integration and the pressure one is intrinsically a low order procedure if not performed with a proper strategy. Some of these studies indicated that is preferable either to adopt multi-step methods or to resort to successive nested iterations (like the Uzawa method). Moreover, the development of a spatially accurate IB method is still in progress because in the classical formulation only a first order accuracy is achieved close to the immersed boundary [12, 26, 27]. In the following section, the previously described numerical procedure is applied in order to simulate the diastole.

5. RESULTS

In order to validate the capability of the model in describing the main physical mechanisms of the filling, the diastole is firstly simulated with normal physiologically parameters.

In order to close the problem, the boundary conditions need to be specified. Dirichlet inflow conditions, i.e. the law describing the flow in the pulmonary veins, are uniformly assigned (see Figure 7) on the two inlets in atrium, according to the experimental data [28]:

$$\mathbf{n}|_p \cdot \mathbf{v} = V_p(t) = \begin{cases} V_{\max} e^{1/2}\dfrac{t\exp(-t^2/2T_{\max}^2)}{T_{\max}} & \text{for } t < T_{ac} \\ c_0 + c_1 t + c_2 t^2 + c_3 t^3 & \text{for } t \geqslant T_{ac} \end{cases} \tag{28}$$

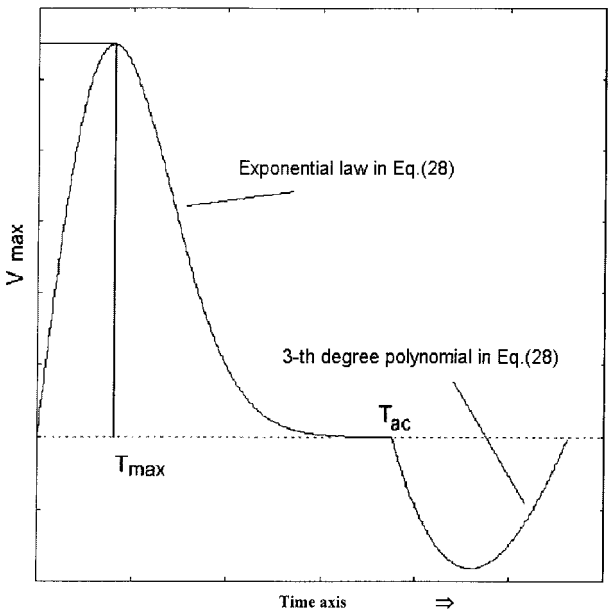

Figure 7. Representation of the time-dependent velocity in Equation (28) adopted as Dirichlet inflow condition on the pulmonary veins. An exponential law for trie early rapid filling and a third degree polynomial for the atrial contraction are adopted.

where $V_{\max}$ is the peak velocity, reached at $T_{\max}$ (the acceleration time of early flow), while T_{ac} is the time of the start of the atrial contraction during which the pulmonary flow reverses, owing to the increasing of the atrial pressure. This reverse-flow is directly imposed on the inlet velocity by using a third order polynomial interpolation, obtained by imposing zero velocity at $t = T_{ac}$ and at the end of contraction $t = T_{\text{end}}$ and by fixing a minimum velocity of $-0.18\,\text{m}\,\text{s}^{-1}$ in the intermediate period, as suggested by clinical experiments.

The atrial contraction is modelled by assuming a suitable uniform normal velocity distribution along the walls of the atrium. As it was already mentioned, it is rather complicated to extract useful numerical boundary conditions from volumes experimental measurements performed during the atrial contraction. Among several velocity distributions that were tested, the best results were obtained by imposing a uniform normal velocity along the atrial walls, modulated in time according to the law

$$\mathbf{n}|_w \cdot \mathbf{v} = V_w(t) = V_{ac} \sin[\pi(t - T_{ac})/(T_{\text{end}} - T_{ac})] \tag{29}$$

where $V_{ac} = 0.1\ \text{ms}^{-1}$.

In order to satisfy the mass balance, as no deformation of the ventricular wall is considered in the model, blood is allowed to flow through the ventricular walls as if the surfaces were permeable. The pressure time-law is imposed along the walls of the ventricle according to experimental measurements obtained by means of catheterism techniques and such law is characterized, at the beginning of diastole, by an exponential decreasing followed by a linear

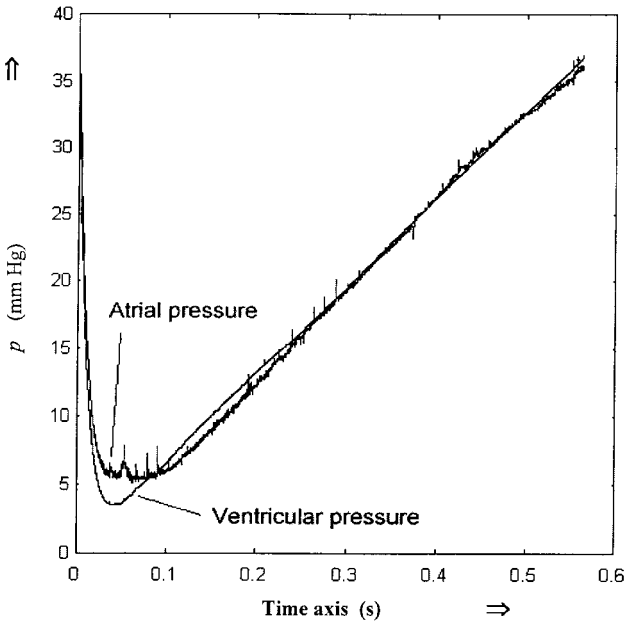

Figure 8. Time representation of the computed atrial pressure and of the ventricular pressure imposed during diastole. Pressure in the ventricle is assigned as an exponential fall law followed by a linear increasing law according to Equation (30). In the plot, pressures are expressed in mm Hg (760 mm Hg $= 1.01325\ 10^5$ N m^{-2}).

increasing caused by rapid filling [1, 2] according to

$$p_v(t) = \frac{p_{0v}}{e}\left[e^{-t/\tau} + \frac{t}{T_{\text{end}}}\right] \tag{30}$$

where τ is the characteristic relaxation time depending on the compliance. As a consequence, the normal components of the velocity on the ventricle are not imposed but they are recovered from the pressure field computation in such a distribution to satisfy the total mass balance.

The reference values of the main geometrical parameters are the following: the diameter of the mitral ring is fixed to 0.032 m and the atrium-to-ventricle apex length to 0.1 m (see Figure 2). The values of the dynamics parameters, adopted for the simulation of a normal case, are: $V_{\max} = 0.55$ m s^{-1}, $T_{\max} = 0.08$ s, $T_{ac} = 0.375$ s, $p_{0v} = 100$ mm Hg, $\tau = 0.01$ s. At the resting condition, each leaflet is described by a suitable parabolic law $y(x)$ and discretized by 40 elements over which the fibre strain is assumed to cause only tension stresses, starting from an assigned length at rest while the *chordae tendineae* tension is computed with respect to the initial arbitrary length. The time integration is performed over a standard normal diastole time period of $T_{\text{end}} = 0.53$ s at a Courant number of 0.1.

The computed atrial pressure and the ventricular pressure, imposed during diastole according to Equation (30), is reported in Figure 8; in the plot, the pressures is expressed in mm Hg (760 mm Hg $= 1.01325 \times 10^5$ N m^{-2}) and the time t in seconds. It is noticeable that, owing to the early filling, the computed left atrial pressure becomes lower than the ventricular one. The average pressure gradient decreases and, transiently, reverses (for $t > 0.1$ s the pressure

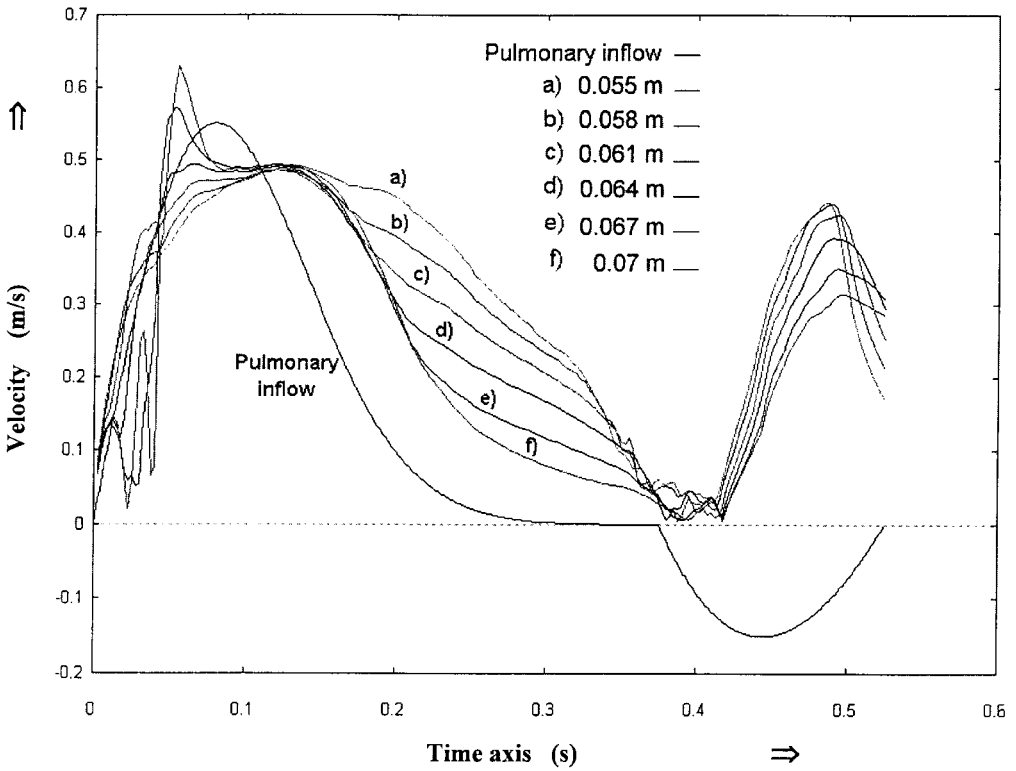

Figure 9. Patterns of E-A waves for the normal case computed at different locations (a)–(f) along the control line (atrium–ventricle line illustrated in Figure 2).

in the atrium becomes lower than in the ventricle) according to the real physical behaviour during the slow filling. Then, the atrial contraction (modelled by means of the normal velocity distribution) increases the pressure late in diastole ($t > 0.4$ s), producing blood to flow again in the left ventricle, according to the A wave shown in Figure 1(a). In order to compare numerical and experimental results, the time evolution of the stream-wise flow is recorded at several locations along a control line extending for 0.05 m in the heart section. Such control line is positioned between the tips of the mitral leaflets, the first station being located in the atrium at $y = 0.03$ m, crosses the mitral ring and extends up to the initial part of the ventricle ($y = 0.08$ m, see Figure 2); in this way, a map of the quantities in the (t, y) plane can be computed and compared with clinical measurements obtained by the M-mode colour Doppler. Rigorously speaking, a quantitative comparison is not possible because the 2-D numerical quantities are expressed for unit area, while experimental measurements are expressed in terms of volume units.

The patterns of E-A waves, computed at different locations ((a)–(f)) along the control line (the atrium-to-ventricle line illustrated in Figure 2), are reported in Figure 9. For sake of completeness the curve of the assigned pulmonary inflow velocity is also reported. These patterns confirm a good agreement with the experimental E-A waves and the shift of velocity maximum, at each time, is captured.

In Plate 1(a)–(d), the velocity vectors and the mitral leaflets movement are plotted during the rapid filling, while in Plate 1(e)–(h) they appear during the slow filling and the atrial contraction. In (a) and (b) the onset of the diastole with a great part of blood flowing into the ventricle is evident while, in (c) and (d), it appears that vortices are formed at the tips of the valve leaflets, being the vorticity produced along the immersed line; these vortices dominate the flow pattern (e) and (f), leading to a partial closure of the mitral valve. In (g) and (h) it appears that the atrial contraction, re-opening the mitral valve, causes blood to flow again into the ventricle with a generation of new vortices.

Let us note that the velocity vectors, appearing to cross the leaflets, do not violate the non-permeable condition but they are only an expression of the fact that the leaflets move at the local fluid velocity. Although the velocity vector field is not fully representative of a real 3-D case, the physics of diastole seem to be correctly captured, even for the mechanism of closure.

A velocity magnitude map in the (t, y) plane is obtained by joining single E-A waves, measured at different locations, and is reported in Plate 2(b); the stream-wise value is recorded on the stations ranging, from bottom to top of the figure, between 0.03 m to 0.08 m.

In order to test the model sensitivity to the perturbation of some physiological parameters, the values of $T_{\max}$ was slightly modified. Firstly it was decreased to 0.07 s (the result is reported in Plate 2(a) wherein the black line individuates the mitral plane) and then it was increased to 0.09 s (Plate 2(c)). As a result of this parameter modification, a strong variation, both of the area characterizing the filling and the corresponding peak velocity, is highlighted. This is relevant information from a clinical point of view [1, 2], being the parameter $T_{\max}$ a Doppler index indicating the inertia in the valve opening.

A qualitative comparison with an experimental M-colour Doppler measurement is reported in Plate 3, where the experimental velocity map in the (t, y) plane was recorded from the equipment, without any signal filtering, and is reported in Plate 3(c). In Plate 3(c) the signal was first processed by means of a convolution with a proper filtering function, while in Plate 3(b) the numerical result in a normal case is reported. The y-range of the experimental measurement is limited from 0.045 m to 0.08 m while the time range is $(0\text{ s}, 0.6\text{ s})$. The good qualitative agreement with clinical data, reached for the normal case, suggests that the simplifications assumed in this model can be considered satisfactory, accomplishing the target of describing the main physical mechanism of diastole.

6. CONCLUSIONS

The present study was devoted to the development of the Immersed Boundary Method on 2-D unstructured grids with the aim of simulating the diastolic phase of the cardiac cycle by using a simplified physical model. The difficulties in simulating such a problem are originated by several elements; some of them are related to the numerical accuracy (mass conservation near the immersed boundaries), others to the incertitude in boundary conditions not obtainable from clinical measurements. In order to close the system of equations, approximate boundary conditions were tested to validate their influence on the physics of the problem.

For what it concerns the numerical method, an explicit single step time marching Finite Volume scheme was implemented in the framework of the fractional time-step procedure.

In order to face the poor spatial accuracy of the method near an immersed line, the new element, introduced in this paper, is the implementation of the method on unstructured grids instead of using nested-refined structured ones that were highlighted in other works. The dynamic of the mitral valve was simulated by adopting a Lagrangian approach and the stresses were spread on the Eulerian grid by means of a discrete point-wise mapping function. An accurate flux reconstruction, adopted on Finite Volumes of general shape, was developed in an original formulation: a proper deconvolution procedure for obtaining a better representation of the volume-averaged velocity was introduced for unstructured grids.

In order both to reproduce a normal function and to test the model sensitivity to changes of physiological parameters, different simulations were performed. The numerical results confirmed the good agreement between the simulation and the real ventricular filling. The physiological normal case was qualitatively compared to a clinical experimental measurement obtained by Doppler analysis and it showed a good agreement in the filling function. Although a fully 3-D simulation is required for quantitative comparisons, nevertheless the simplified 2-D model can help clinicians in evaluating the physical implications of some experimental Doppler indices.

ACKNOWLEDGEMENTS

This paper is part of collaboration with haemodynamics clinicians; the authors want to thank Dr sa C. Capozzolo and Dr G. Tonti for the useful clinical observations, and Prof. G. Riccardi for helpful discussions on the mathematical model. Furthermore, many thanks go to Prof. C. S. Peskin who kindly provided an upgrade of his recent publications on the immersed boundary method and to B. Raucci who is a student preparing his dissertation thesis on the IB method.

REFERENCES

1. Yellin EL, Nikolio S, Frater RWM. Left ventricular filling dynamics and diastolic function. *Progress in Cardiovascular Diseases* 1990; **XXXII**:4.
2. Thomas JD, Choong CYP, Flachskampf FA, Weyman AE. Analysis of the early transmitral Doppler velocity curve: effect of primary physiologic changes and compensatory pre-load adjustment. *Journal of American College of Cardiology* 1990; **16**:3.
3. Thomas JD, *et al*. Spatio-temporal distribution of mitral flow velocity: use of Doppler M-mode echocardiogram to investigate intra-cardiac pressure gradients. *Medical and Biological Engineering Computing* 1991; **29**:130.
4. Yamamoto K, *et al*. Intraventricular dispersion of early diastolic filling: a new marker of left ventricular diastolic. *American Heart Journal* 1995; **129**:291–299.
5. Pedley TJ. *The Fluid Mechanics of Large Blood Vessels*. Cambridge University Press: Cambridge, 1980.
6. Peskin CS. Numerical analysis of blood flow in the heart. *Journal of Computational Physics* 1977; **25**.
7. McQueen DM, Peskin CS, Yellin EL. Fluid dynamics of the mitral value: physiological aspects of a mathematical model. *American Journal of Physiology* 1982; **242**.
8. Peskin CS, McQueen DM. A three-dimensional computational method for blood flow in the heart I. Immersed elastic fibers in a viscous incompressible fluid. *Journal of Computational Physics* 1989; **81**.
9. Peskin CS, Printz BF. Improved volume conservation in the computation of flows with immersed elastic boundaries. *Journal of Computational Physics* 1993; **105**.
10. Peskin CS, McQueen DM. Computational biofluid dynamics. *Contemporary Mathematics* 1993; **141**.
11. Peskin CS, McQueen DM. *A General Method for the Computer Simulation of Biological Systems Interacting with Fluids*. The Society for Experimental Biology, 1995; **265**.
12. Roma AM, Peskin CS, Berger MJ. An adaptive version of the immersed boundary method. *Journal of Computational Physics* 1999; **153**:509–534.
13. Pilkington TC, Lofts B, Thompson JF, Woo SL-Y, Palmer TC, Budinger TF (eds). *Cray Symposium on High-Performance Computing in Biomedical*. North Carolina Supercomputing Center at Research Triangle Park, North Carolina, CRC Press, 1993.
14. Ye T, Mittal R, Udaykumar HS, Shyy W. An accurate Cartesian grid method for viscous incompressible flows with complex immersed boundaries. *Journal of Computational Physics* 1999; **156**:209–240.

15. De Felice G, Denaro FM, Meola C, Sarghini F. Model free numerical simulation of high Reynolds compressible flows on adaptive unstructured grid. *Conference of Numerical Method for Fluid Dynamics*, Oxford, 3–6 April, 1995.
16. Denaro FM. Toward a new model-free simulation of high Reynolds flows: local average direct numerical simulation. *International Journal for Numerical Methods in Fluids* 1996; **23**:125–142.
17. Sarghini F. Simulazioni ai Volumi di Controllo per Campi Compressibili Subsonici su Griglie Non Structturate, Basate su Tecniche di Ricostruzione delle Variabili Dirette e Filtrate, Tesi di dottorato, Facoltá di Ingegneria, Universitá 'Federico II' di Napoli, Italy, 1996.
18. De Stefano G, Denaro FM, Riccardi G. Analysis of 3-D backward facing step incompressible flows via a local average-based numerical procedure. *International Journal for Numerical Methods in Fluids* 1998; **25**.
19. Chorin AJ. Numerical solution of the Navier–Stokes equations. *Mathematical Computations* 1968; **22**:745–762.
20. Almgren AS, Bell JB, Szymczak WG. A numerical method for the incompressible Navier–Stokes equations based on the an approximate projection. *SIAM Journal on Science and Computing* 1996; **17**:358–369.
21. Perot JB. An analysis of the fractional step method. *Journal of Computational Physics* 1993; **108**:51–58.
22. E W, Liu JG. Projection method I: convergence and numerical boundary layers. *SIAM Journal on Numerical Analysis* 1995; **32**(4):1017–1057.
23. Strikwerda JC, Lee YS. The accuracy of the fractional step method. *SIAM Journal on Numerical Analysis* 1999; **37**(1):37–47.
24. Brown DL, Cortez R, Minion ML. Accurate projection methods for the incompressible Navier–Stokes equations. *Journal of Computational Physics* 2001; **168**.
25. Chorin AJ. On the convergence of discrete approximations to the Navier–Stokes equations. *Mathematical Computations* 1969; **23**:341–353.
26. Leveque RJ, Li Z. Immersed interface methods for Stokes flow with elastic boundaries or surface tension. *SIAM Journal on Science and Computing* 1997; **18**:709–735.
27. Stockie JM, Wetton BR. Analysis of stiffness in the immersed boundary method and implications for time-stepping schemes. *Journal of Computational Physics* 1999; **154**:41–64.
28. Tonti G, Fedele F, Mantredi RM, Trambaiolo P, Capozzolo C, Denaro FM, Riccardi G. Numeric models for supporting noninvasive investigation of the left atrium–ventricle system. *Journal of Cardiovascular Diagnosis and Procedures*. Mary Ann Libert Inc. Publ: Larchmont, Win, 1998; **15**(4):285–293.
29. Capozzolo C, Denaro FM, Sarghini F. Transmitral flows analysis by means of computational fluid dynamics on unstructured grids. *Third International Symposium on Computer Methods in Biomechanics and Biomedical Engineering*, 7–10 May 1997, Barcellona, Spain.
30. Fung YC. *Biodynamics: Circulation*. Springer-Verlag: New York,1984.
31. Shyy W, Udaykumar HS, Rao MM, Smith RW. Computational fluid dynamics with moving boundaries. *Computational and Physical Processes. in Mechanics and Thermal Sciences*, University of Florida, Gainesville, FL. Taylor & Francis, 1995.
32. Denaro FM, De Stefano G, Riccardi G. Local-average based numerical simulation of turbulent flows. *First AFOSR International Conference on Direct Numerical Simulation and Large Eddy Simulation* (*DNS*/*LES*), Louisiana Tech University, Ruston, Louisiana, U.S.A., 4–8, 1997.
33. De Stefano G, Denaro FM, Riccardi G. High order filtering formulation for control volumes simulation of turbulent flows. *International Journal for Numerical Methods in Fluids* 2001; **37**:4.
34. de Felice G, Denaro FM, Meola C. Multidimensional single step vector upwinded schemes for highly convective transport problems. *Numerical Heat Transfer*, *Part B* 1993; **23**:4.
35. Kantorovic LV, Akilov GP. Analisi Funzionale, *Ed. MIR*, 1980.
36. Chorin AJ, Marsden JE. *A mathematical Introduction to Fluid Mechanics. Texts in Applied Mathematics* 4. Springer-Verlag: New York, 1990.

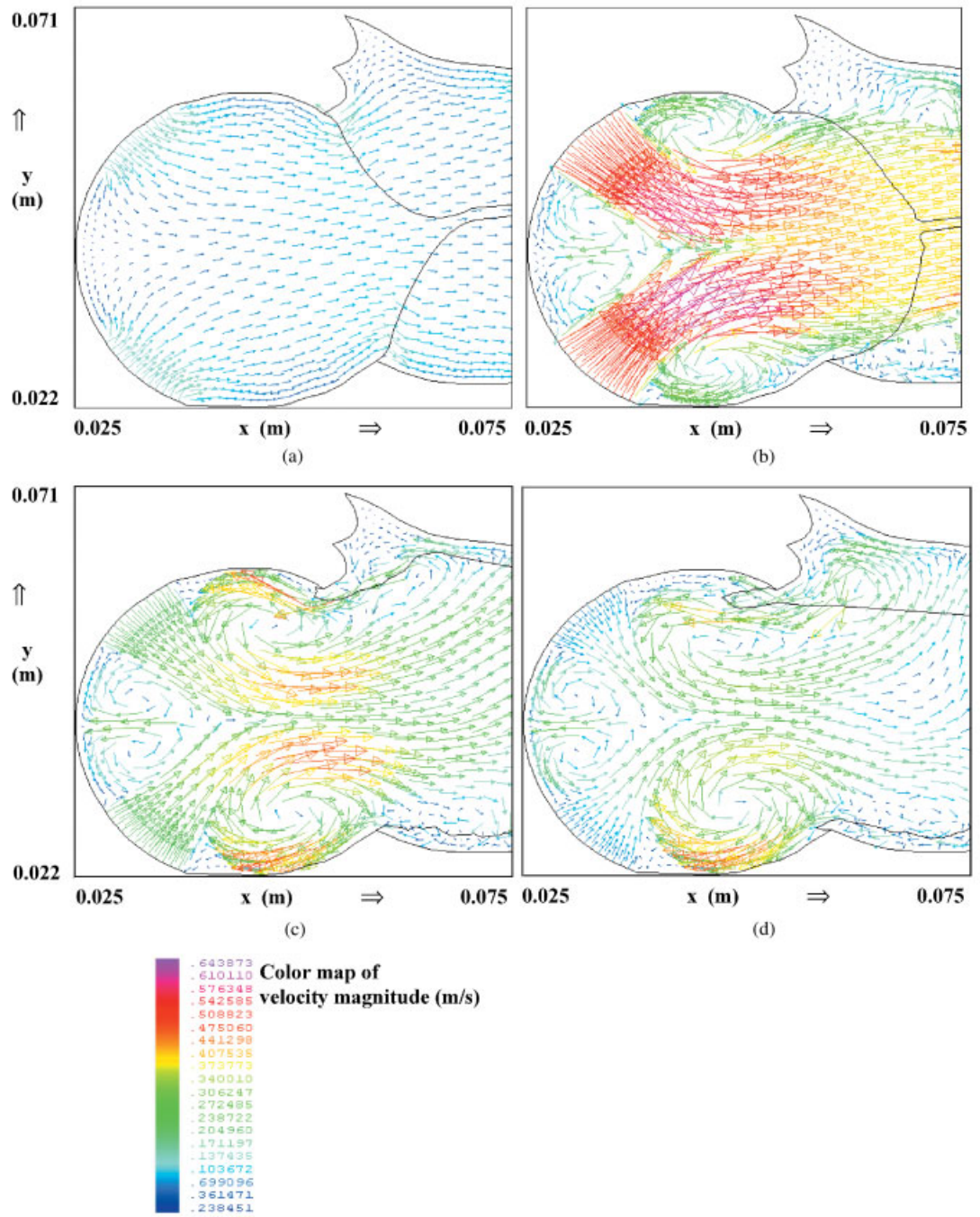

Plate 1. (a–d) Computed velocity vectors and dynamic of the mitral leaflets during (a)–(d) the rapid filling, (e)–(h) the slow filling and the atrial contraction.

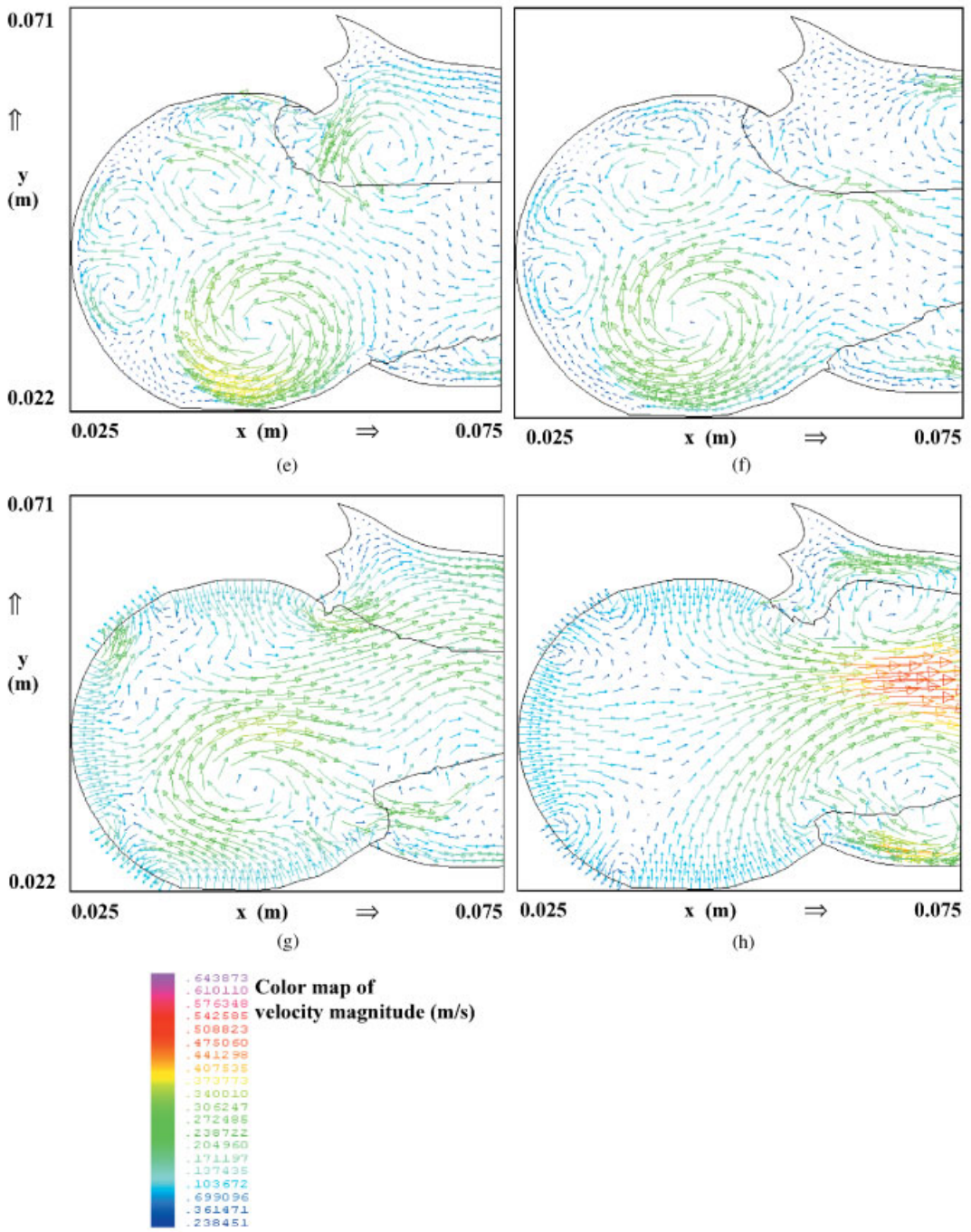

Plate 1. *Continued.*

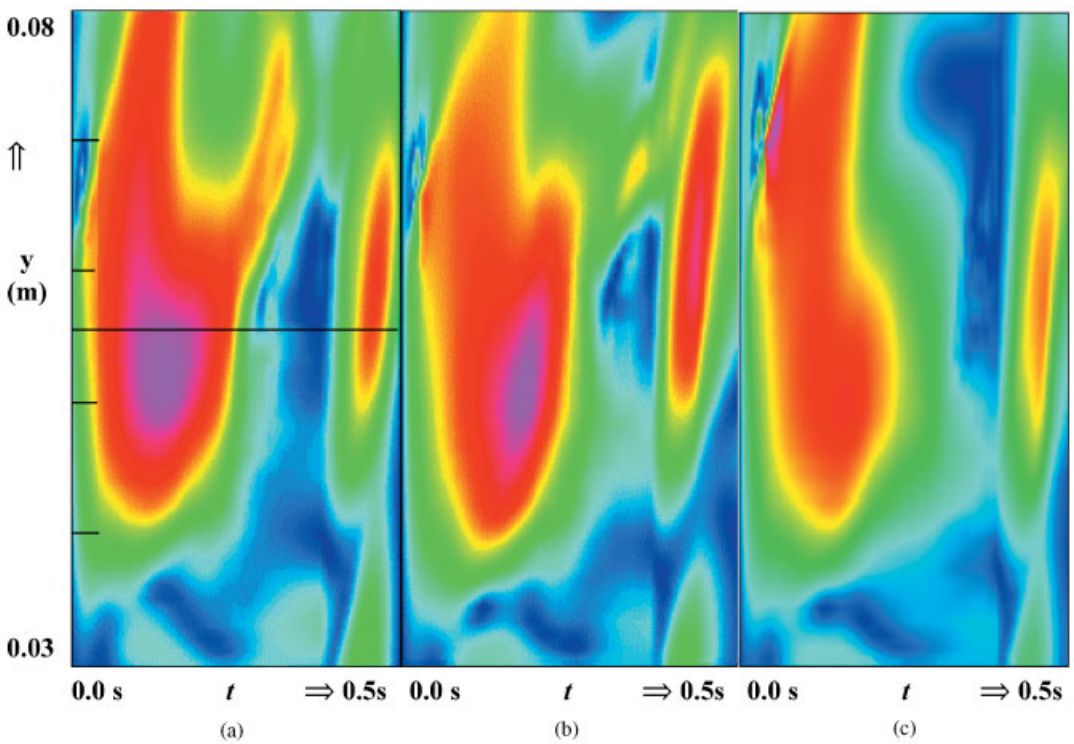

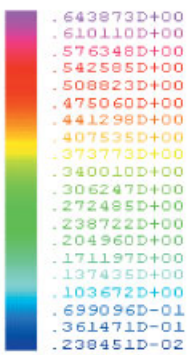

Color map of velocity magnitude (m/s)

Plate 2. Velocity magnitude maps in the (t, y) plane. For each figure the time is expressed in seconds along the x-direction. In the y-direction, the stream-wise value (along the control line of Figure 2) ranging, from bottom to top of the figures, between 0.03 m to 0.08 m, is registered. Colour map scale magnitude is in $\mathrm{m\,s^{-1}}$. The black line on (a) individuates the mitral plane. In (a) $T_{\max} = 0.07\,\mathrm{s}$, (b) (normal physiological case) $T_{\max} = 0.08\,\mathrm{s}$. (c) $T_{\max} = 0.09\,\mathrm{s}$.

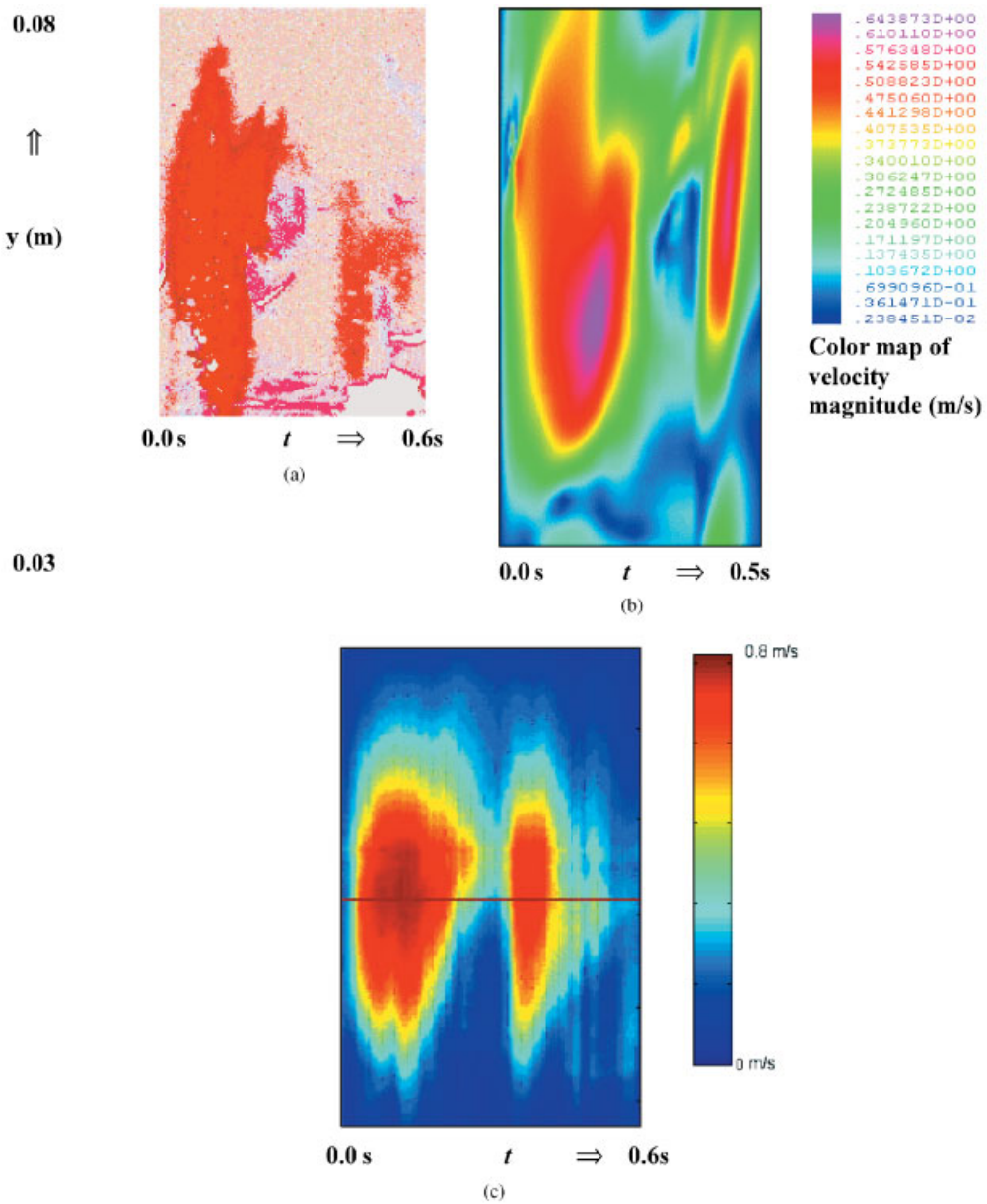

Plate 3. Velocity magnitude maps in the (t, y) plane. In (b) it is again reported the numerical result of the normal case of Figure 11(b). In the y-direction, the stream-wise value (along the control line represented in Figure 2) ranging, from bottom to top, between 0.03 m to 0.08 m, is registered. The y-range of the experimental measurement obtained with the M-mode colour Doppler, is limited between 0.045 m to 0.08 m while the time range is (0 s, 0.6 s).